Engineering Geology 101 (2008) 15–32

Contents lists available at ScienceDirect

Engineering Geology

journal homepage: www.elsevier.com/locate/enggeo

Internal structure and deformation of an unstable crystalline rock mass above Randa (Switzerland): Part II — Three-dimensional deformation patterns

Heike Willenberg [a], Keith F. Evans [a], Erik Eberhardt [a,1], Thomas Spillmann [b,2], Simon Loew [a,*]

[a] Geological Institute, Swiss Federal Institute of Technology, ETH Hoenggerberg, Zürich, Switzerland
[b] Institute of Geophysics, Swiss Federal Institute of Technology, ETH Hoenggerberg, Zürich, Switzerland

ARTICLE INFO

Article history:
Received 25 June 2007
Received in revised form 18 January 2008
Accepted 26 January 2008
Available online 23 February 2008

Keywords:
Rockslide
Monitoring
Inclinometer
Kinematics

ABSTRACT

The monitoring of slope displacements over time provides the basis for most rockslide early warning systems, yet the prediction of catastrophic failure from these records is highly problematic and tenuous, especially if the underlying kinematics and instability mechanism are poorly understood. An example is the moving slope above the town of Randa in the Swiss Alps. This slope is considered typical of those in crystalline rock that lacks a natural, highly persistent, weakness plane dipping towards the valley that can serve as a through-going detachment surface for kinematic release. In Part I (the companion paper to this), the findings from a comprehensive geological and geophysical investigation to image the internal structures of the unstable rock mass were presented. In this paper we develop a kinematic model that describes the pattern of displacement vectors for the rock mass along these structures, both on surface and at depth. The displacements were estimated from 5 years of data from an extensive monitoring system which included surface geodetic and crackmeter measurements, borehole inclinometer and extensometer measurements (up to 120 m depth), and microseismicity. The results showed that the displacement field is highly heterogeneous. Internal deformation is accommodated by both shear and opening-mode dislocation of faults and fracture zones which dip moderately to steeply into the slope. Microseismicity is most intense near the front of the scarp where surface translation in large part reflects the toppling of blocks accommodated by slip along the steeper dipping fractures. The small displacement rates at the study site of up to 2 cm/year coupled with a modest deviation of up to 15° from vertical of the boreholes posed severe problems for the estimation of horizontal displacements from the inclinometer data. We describe the error analysis of these data in some detail since it is relevant for similar installations elsewhere. Conclusions drawn from this work highlight the importance of integrating various types of data in order to better understand the complex block-kinematic processes whose evolution governs the long-term progressive failure of unstable rock slopes.

1. Introduction

Landslide hazard mitigation in Alpine areas has increasingly involved the deployment of early warning systems (Eyer et al., 1998; Brasser and Gruner, 2002; Keusen, 2002). These are usually based upon monitoring of slope displacements over time to detect accelerations that may be indicative of catastrophic failure (e.g. Fukuzono, 1985; Voight, 1989; Crosta and Agliardi, 2002). The interpretation of such data is often not straightforward, as seasonal variations, and complex internal processes driven in part by the slowly-changing geometry and structure of the moving slope, can give rise to intermittent velocity changes. The identification of hazardous changes could be significantly improved if the underlying mechanisms leading to failure were properly understood (e.g. Rose and Hungr, 2007). This is particularly true for cases where the geological structure does not accommodate a straightforward kinematic mode of failure, for example the presence of adversely dipping, highly persistent planes of weakness (e.g. bedding planes or foliation) that either dip out of or into the slope enabling translational sliding or flexural toppling, respectively. If the discontinuity network is more random in orientation, spacing and persistence, the failure surface is obliged to develop in a progressive

* Corresponding author.
E-mail address: loew@erdw.ethz.ch (S. Loew).
[1] Present address: Geological Engineering/EOS, University of British Columbia, Vancouver, BC, Canada.
[2] Present address: National Cooperative for the Disposal of Radioactive Waste/Nagra, Wettingen, Switzerland.

0013-7952/$ – see front matter © 2008 Elsevier B.V. All rights reserved.
doi:10.1016/j.enggeo.2008.01.016

manner, stepping up and through the rock mass linking smaller-scale non-persistent discontinuities before large scale failure can occur.

Case studies in which the surface and sub-surface displacements of an unstable rock mass are monitored during the lead-up to failure can provide insights into the key processes that control the progression towards failure. Most studies of rockslide displacements are limited to surficial measurements, such as the opening of tension cracks (e.g. Sandersen et al., 1996; Bogaard et al., 2000; Krähenbühl, 2004; Gunzburger et al., 2005), the movement of geodetic reflectors and/or GPS tracking (e.g. Brückl et al., 2006) and more recently, the employment of ground-based and satellite radar interferometry methods (e.g. Canuti et al., 2002; Tarchi et al., 2003; Colesanti and Wasowski, 2006). Studies which include displacements monitored at depth are usually concerned with open pit mine slopes (Ding et al., 2000) or dam reservoir slopes (Imrie and Moore, 1993; Watson et al., 2004). However, several rockslide investigation programs have recently been initiated which involve the monitoring of diverse parameters on the surface and underground (Willenberg et al., 2002; Blikra et al., 2005; Froese et al., 2005; Groneng et al., 2005), including microseismicity (Blikra et al., 2005; Brückl and Parotidis, 2005; Spillmann et al., 2007a).

This paper describes the results obtained from the first of these multifaceted systems, the Randa In-Situ Rockslide Laboratory that was set up on a moving rock mass 1000 m above the village of Randa in the Swiss Alps. The rock mass lies immediately above the scarp of a major multiple rockslide event that occurred in 1991. Internal deformation of the rock mass was monitored with boreholes equipped with inclinometer and extensometer systems. Surface deformation was monitored with an extensive array of geodetic and fracture-dislocation measurements. Here we analyse the data and integrate the results with those from the geological model developed in Part I, the companion to this paper, to derive a block-kinematic model for the unstable rock mass.

2. Background

The study area for the Randa In-Situ Rockslide Laboratory was sited above the scarp of the 1991 Randa rockslide in southern Switzerland, where 30 million m^3 of rock failed during two large events three weeks apart, producing a 1000 m high scarp (see Figs. 1–3 in Part I). Since these events, the slope above the scarp has been moving towards the SE at a maximum velocity of 2 cm/year (Jaboyedoff et al., 2004; Ornstein et al., 2005). The rock mass is composed of a series of gneisses and schists whose foliation dips 25° to the west, which is into the slope, thereby favouring stability. Geological mapping and geophysical investigations showed that the moving rock mass hosts a higher density of faults and fracture zones than the surrounding medium (Willenberg, 2004; Heincke et al., 2006a,b; Spillmann et al., 2007b). These fall into three primary sets: F-1 is a family of brittle–ductile shear zones that lie parallel to the foliation plane; F-2 are high-to-moderate angle faults and fracture zones that, exhibiting more dispersion, dip between north and northwest; and F-3 are faults and fracture zones that strike N–S and dip steeply to the east. Fig. 1 shows the surface traces of faults belonging to sets 2 and 3. Most faults and fracture zones have substantial lateral extent and can be traced on radar images to depths of up to 80 m. They thus dissect the rock mass into a complex assemblage of blocks with sizes ranging from 7 to 30 m (Willenberg, 2004). Importantly, no fault or fracture zones were found that dip shallowly to the SE, i.e. sub-parallel to the general displacement direction of the moving rock mass. If these structures were present, then the measured slope movements could probably be easily explained using a simple kinematic model involving translational sliding and shear. One set of fractures with limited persistence ($\ll$10 m) were found in this orientation, but their density and persistence is insufficient to form a stepped sliding surface without extensive shearing of intact rock. Thus, the manner in which the observed surface displacements are accommodated within the rock

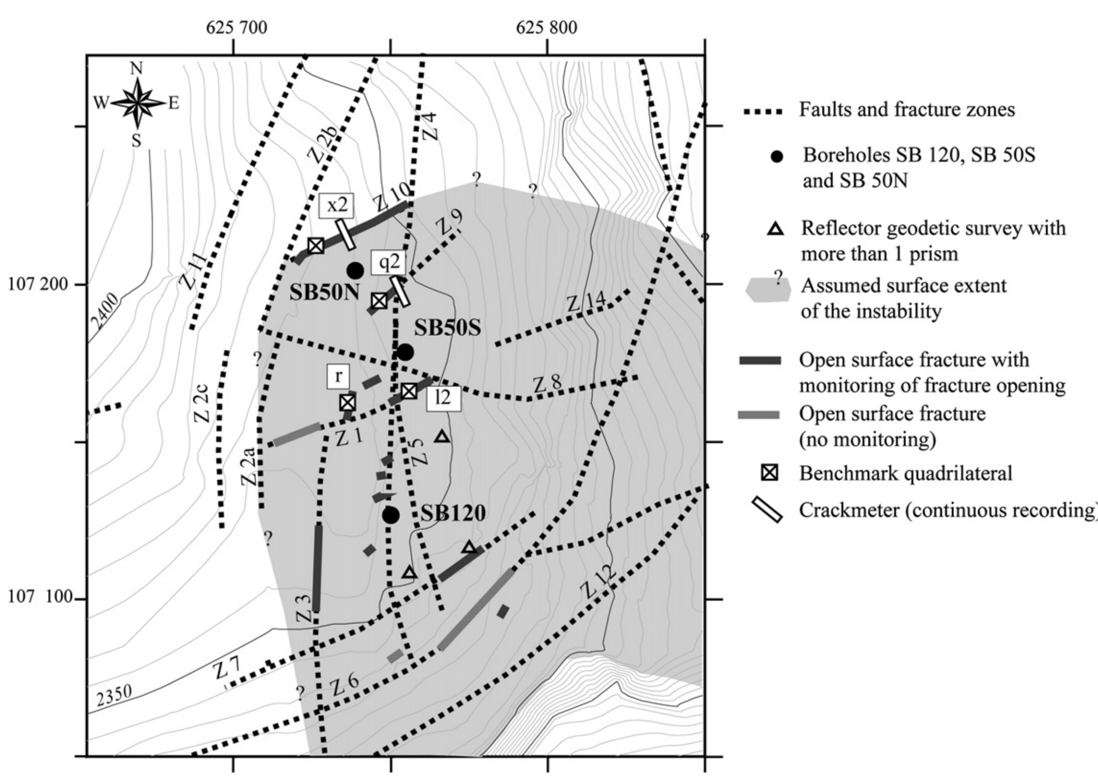

Fig. 1. Overview of the study area showing components of the monitoring network and surface traces of the F-2 and F-3 fault sets (see Fig. 10 in Part I for strike and dip). Open fractures on surface are shown as solid lines on the inferred fault network (dashed lines). The filled circles denote the locations of the three deep boreholes. The contour interval is 5 m.

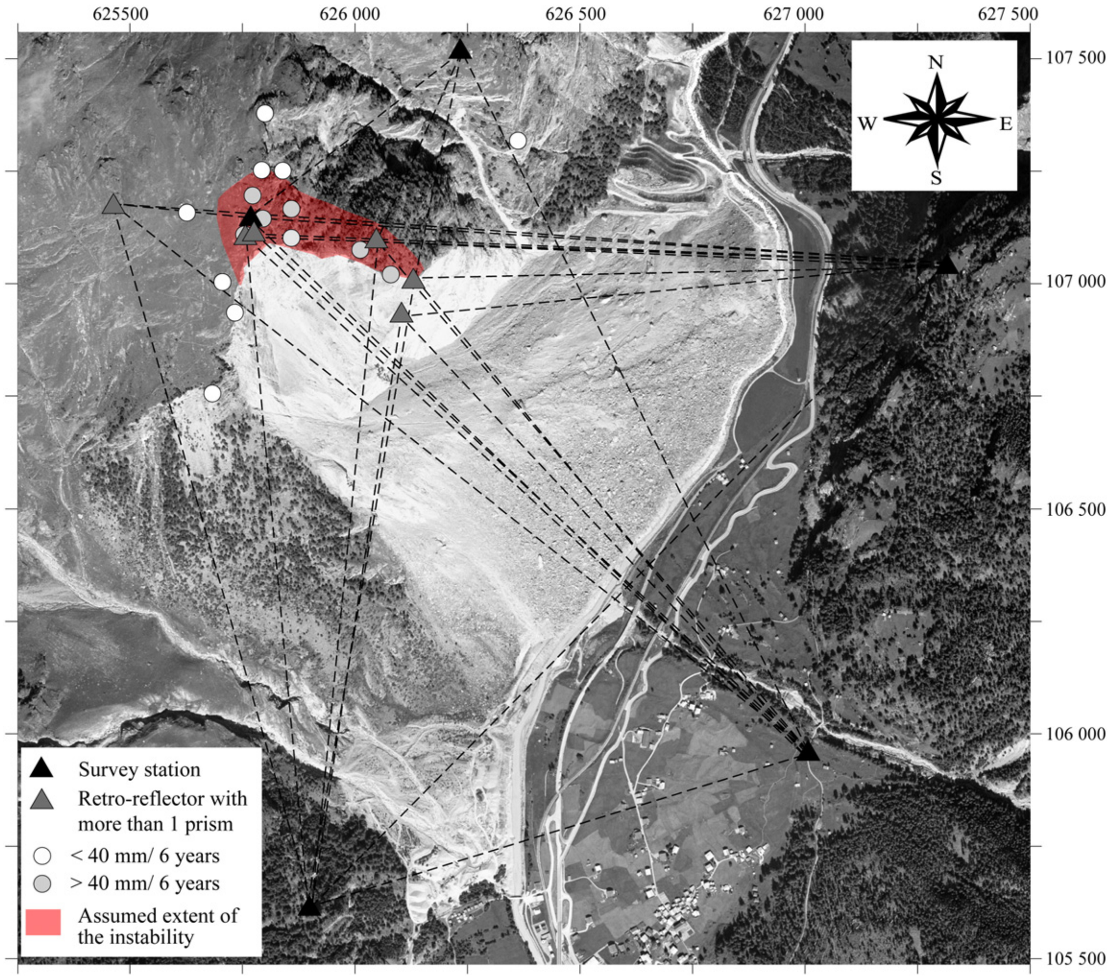

Fig. 2. Geometry of the geodetic survey system (modified after Ornstein et al., 2005) projected onto an orthophoto of the area (reproduction permit BA068088 by swisstopo). Monitoring points involving a single prism are indicated by circles. Following Jaboyedoff et al. (2004), they are shown as having little or no displacement (white circles) or displacements of more than 4 cm accrued over 6 years (grey-filled circles). Retro-reflectors with 2–3 prisms are indicated by grey triangles, with black triangles marking the position of the base stations. The estimated extent of the present day instability is shown shaded and is based on the results of the geodetic survey 1991–2000 presented in Jaboyedoff et al. (2004).

mass (i.e. through-going basal sliding or complex internal deformation) is uncertain.

In 2001, the Randa In-Situ Rockslide Laboratory was established through a comprehensive expansion of the existing monitoring system established after the 1991 rockslides (Ornstein et al., 2005). The components of these two systems are listed in Table 1. The aim of the In-Situ Laboratory was to provide information about the geologic structure, internal deformation, microseismicity and pore pressure characteristics of the moving rock mass. Three boreholes, hereafter denoted SB 120, SB 50S and SB 50N (Fig. 1), were drilled to depths of 120, 50 and 50 m, respectively. All holes remained dry, except for the lowermost 10 m of SB 120. The borehole walls were sufficiently stable to allow optical televiewer, borehole geometry and spectral gamma logs to be run, and cross-hole, single-hole and borehole-to-surface radar and seismic surveys to be conducted (see Part I). After their completion, PVC inclinometer casing equipped with 3-component geophone and piezometer modules was grouted into the boreholes, the casing in SB 120 being additionally fitted with an INCREX extensometer system. The monitoring of prominent open fractures at the surface was expanded and improved, and the borehole tops integrated into the geodetic network (in 2002). The microseismic system involved a 12-station array comprised of both shallow and deep sensors (Spillmann et al., 2007a).

3. Geodetic monitoring

The results of the valley-scale geodetic network are important because they provide a framework of absolute displacements that helps in the interpretation of the various deformation measurements in the study area. The geodetic network that has been in operation since 1995 is shown in Fig. 2. Line-length and angle measurements between the 3-prism retro-reflectors were performed semi-annually 1996–1999 and annually since then by the company Klaus Aufdenblatten of Zermatt who also analysed the data. Since 2002, the tops of the boreholes were included in the surveys by determining their position with respect to nearby stations.

Fig. 2 also shows the assumed extent of the unstable rock mass based on the geodetic survey results reported 1991–1997 by Jaboyedoff et al. (2004). Station coverage determines the boundary of the moving rock mass to the north fairly precisely, but its extent to the west and northeast is poorly constrained. The displacement rates increase from zero at the northern boundary to a maximum of 1.8–2.0 cm/year at the edge of the scarp of the 1991 rockslides. A similar distribution of displacement rates is found for the period 1997–2006. The displacement vectors are consistently directed towards the SE, although the dip varies with station from 20° to 50° (Willenberg, 2004). The displacement vectors measured in the study area are shown in plan view in Fig. 3. The absolute displacement

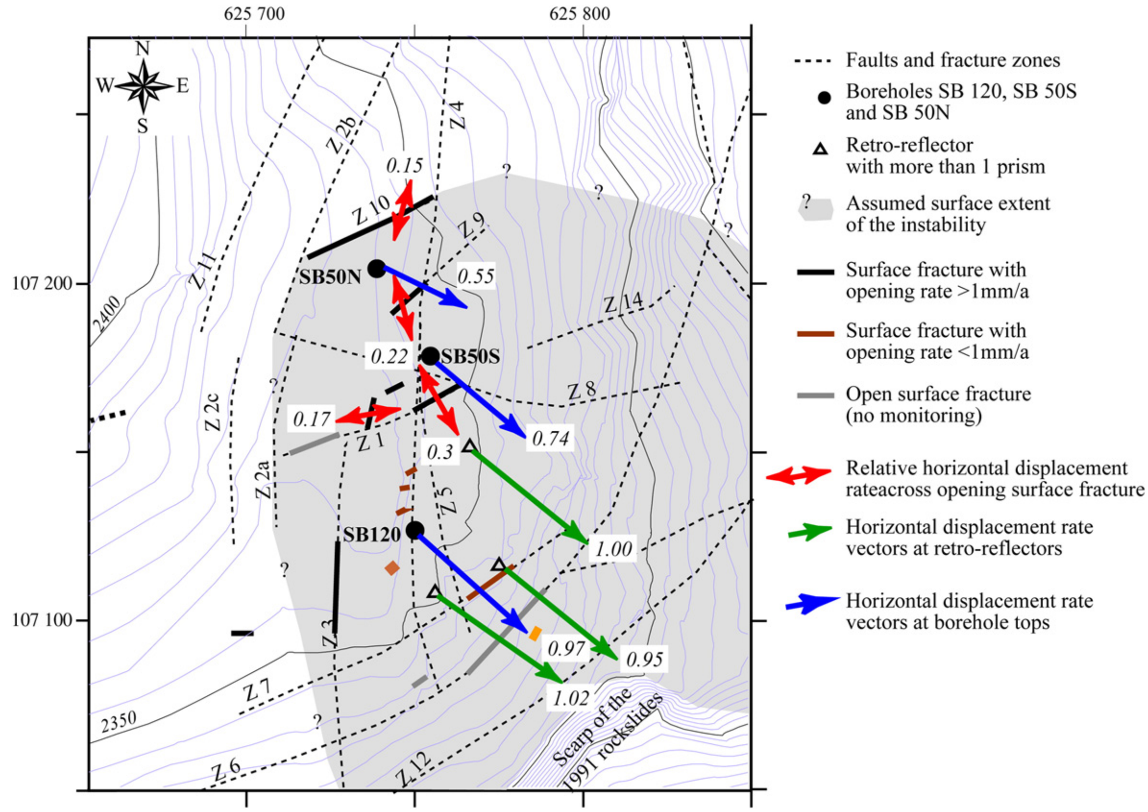

Fig. 3. Surface displacement map showing the horizontal component of the surface displacement rates (cm/year) measured between 2001 and 2005. The assumed extent of the unstable part of the rock mass is shown shaded. Active faults are plotted in black, brown or grey depending on the magnitude of fault opening measured using simple benchmark pairs. The displacement vectors across four of the most active faults (red) were derived from benchmark quadrilateral measurements and indicate the relative displacements of the southern or eastern side with respect to the northern or western side. The displacement vectors of the retro-reflectors of the geodetic survey (green) and the borehole tops (blue) are absolute since they are referenced to an external coordinate system.

vectors of the tops of boreholes SB 120 and SB 50S are essentially consistent with the displacement directions observed at the nearby retro-reflectors.

4. Microseismic monitoring

The microseismic network is shown in plan in Fig. 4. All stations used 3-component geophones, positioned near the bottom of the three deep boreholes and nine shallow boreholes (0.5–5 m deep) drilled for the purpose (Spillmann et al., 2007a). Between 2002 and 2004, a total of 233 locatable events with moment-magnitudes ranging between −1.5 and 0.0 occurred within the study area. Spillmann et al. (2007a) determined their hypocentral location using a 3-D P-velocity model and a probabilistic inversion procedure that accounts for uncertainties in the phase arrival times and the velocity of the various units. The outcome of the procedure for a single event is a probability density function (PDF) that describes the localisation and related uncertainties of the hypocentre. Its value at a given point

Table 1
Components of the monitoring system installed between 2001 and 2003

Instrument	Type	Number	Sampling period	Operation since	Accuracy
Benchmark pairs	Tape-measure	12	0.5 year	2001	0.5 mm
	Tape-measure	14	0.5–1 year	1991[a]	0.5 mm
Benchmark quadrilaterals	Beam-compass	4	0.5 year	2002 (2003)	0.3–0.5 mm
Surface extensometers	Vibrating-wire	2	6 min	2001	0.15 mm
		7	1 day	1991[a]	
Geodetic survey	Markers at borehole top	3	1 year	2002	
	1 — prism retro-reflector	13	0.5–1 year	1991[a]	
	2 — prism retro-reflector	3	0.5–1 year	1991[a]	
	3 — prism retro-reflector	4	0.5–1 year	1995[a]	Error ellipse: 2 mm (a), 2 mm (b), 6 mm (h)
Inclinometer	Servo-accelerometers		0.5–1 year	2001	0.21 mm (vertical) 0.75 mm (±15° incl.)
Extensometer	Induction-coil transducer		0.5–1 year	2001	0.01 mm
In-place-inclinometer	Vibrating-wire	2	6 min	2003[b]	0.09 mm
Piezometer	Vibrating-wire	3	6 min	2001	1.75.3.5 mbar/°C
Geophones in deep boreholes	3-component (f_n=28 Hz)	3	Event-triggered	2002–2004	
Geophones in shallow boreholes	3-component (f_n=8 Hz)	9	Event-triggered	2002–2004	
Meteo station		1	1 h	1991[a]	

[a] Existing early warning system (Ornstein et al., 2005).
[b] 2001–2003 malfunctioning sensors.

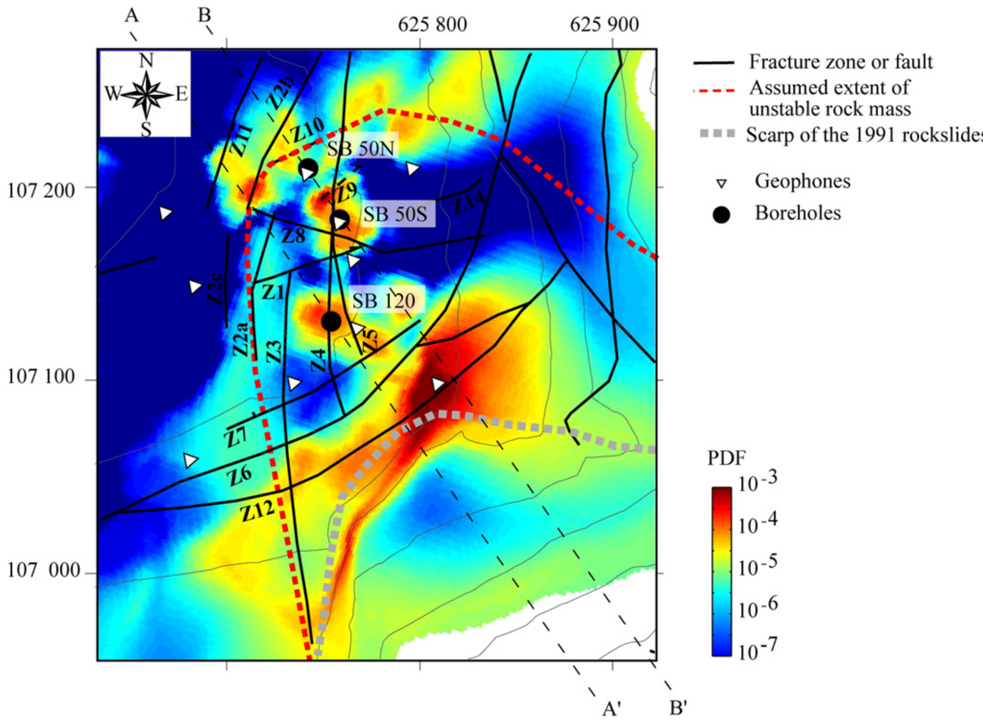

Fig. 4. Map view of the cumulative PDF of the 223 located microseismic events (modified after Spillmann et al., 2007a). Values are plotted on a surface that lies 15 m vertically below the topographic surface shown by the 50 m-spaced contours. Triangles denote the location of geophones and black dots the location of the three deep boreholes. Vertical cross sections along the profiles A–A' and B–B' are presented in Fig. 14.

describes the probability that the event was located within a unit volume centred at that point. The sum of the 223 PDFs of the located events provides a measure of the event density distribution for events with similar uncertainties. The cumulative PDF is shown in Fig. 4 (as well as later in Fig. 14). The distribution shows that the unstable rock mass is deforming/shearing internally. The events are largely confined to the interior of our estimated bounds for the moving rock mass and have the greatest density in the vicinity of the scarp. The distribution is also heterogeneous, with volumes of high event-count density tending to be located near mapped faults and fracture zones. Although the events appear to be largely confined to the uppermost 50 m, this is quite possibly a consequence of the high attenuation created by open fractures. Thus, it is possible that seismic activity extends deeper.

5. Surface fracture monitoring

The relative displacements occurring across prominent open surface fractures, which Fig. 1 shows to be segments of faults and fracture zones, were measured in three ways. The first relied on simple benchmark measurements made perpendicular to the open fractures using a tape measure. These were measured periodically between summer 2001 and autumn 2005. The error in the measurement is estimated at ±0.5 mm (Table 1). The second method was a refinement of the first and used benchmark quadrilateral arrays measured with a purpose-built caliper gauge which reduced the error to ±0.1 mm. This allowed the horizontal relative displacement vector (i.e. normal and shear components) across the fracture to be resolved (Fig. 5). Two approaches were applied to derive relative displacement vectors from the measured line length changes. The first, after Baum et al. (1988), calculates the angles in the triangles ABC, ABC′ and ABD, ABD′ using the cosine law to estimate the horizontal displacement vectors, u_c and u_d of points C and D with respect to the stable baseline AB (Fig. 5). The second approach used a grid search approach to find the single horizontal displacement vector which best reproduced the linear strains AC′–AC, BC′–BC, BD′–BD and AD′–AD. The third method involved continuous monitoring using a Geokon vibrating-wire crackmeter (extensometer) to determine the temporal characteristics of fracture opening. Two fractures (q2 and x2 in Fig. 1) were instrumented in autumn 2002 and the signal logged every 6 min.

The cumulative relative displacement vectors at the four sites instrumented with benchmark quadrilateral arrays are shown in Fig. 6. The direction of opening in plan view is indicated in Fig. 3. The

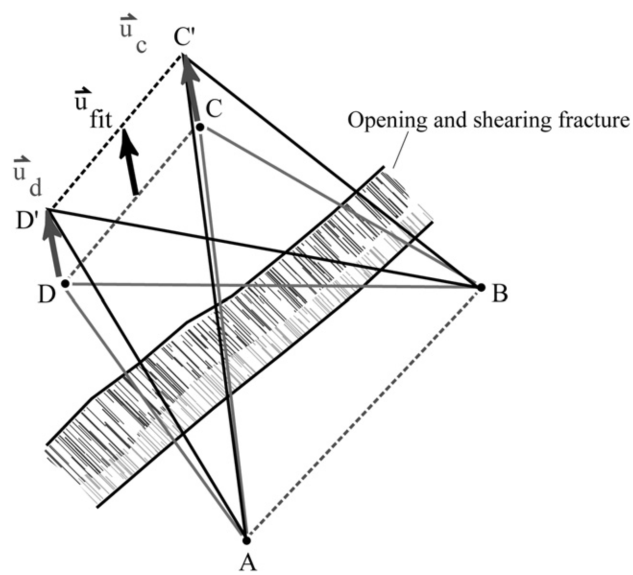

Fig. 5. Illustration of benchmark quadrilateral measurements, made between facing and diagonal benchmarks. The initial quadrilateral geometry, ABCD, is delineated in grey and the deformed quadrilateral, ABC'D', in black. Dashed lines denote benchmark pairs whose distances are measured once at the initial survey.

fracture opening estimates for the benchmark quadrilaterals are slightly dependent on the method used for the analyses. These differ because of systematic errors arising from the slight non-planarity of the array, and possibly the presence of secondary fractures cutting the array at x2. Relative displacement rates obtained from the long-term trends after removal of any annual fluctuations range between 1.5 mm/year at 'x2' to 3 mm/year at 'l/l2'. Openings at faults x2 and q2 were seen to have a significant horizontal shear component (Fig. 6).

A comparison of the results obtained from all three methods for faults x2 and q2 is shown in Fig. 7. Crackmeter records, benchmark quadrilateral arrays and the simple benchmark pair measurements show a large seasonal fluctuation of up to several millimeters This fluctuation is undoubtedly real and is most probably dominated by shallow thermo-elastic strains driven by the annual temperature cycle (Berger, 1975; Harrison and Herbst, 1977). However, a component of deeper rock mass deformation that is periodic may also be present. An approximately linear trend to the displacements of ~2 mm/year can be seen superimposed on the annual cycles. These trends almost certainly have a more deep-seated origin than the annual thermo-elastic signal, and most likely reflect downslope deformation of the rock mass. The data in Fig. 7 also demonstrate that fracture opening estimates from the benchmark arrays and crackmeters tend to agree. The decidedly lower displacement rate inferred for the benchmark quadrilateral at x2 is probably due to its distance (several meters) from the co-located crackmeter/benchmark pair, and thus indicates variability in relative displacement along the fault.

6. Borehole monitoring

6.1. Methods

Fig. 8 shows the positioning of the borehole geotechnical and microseismic monitoring systems listed in Table 1. The borehole

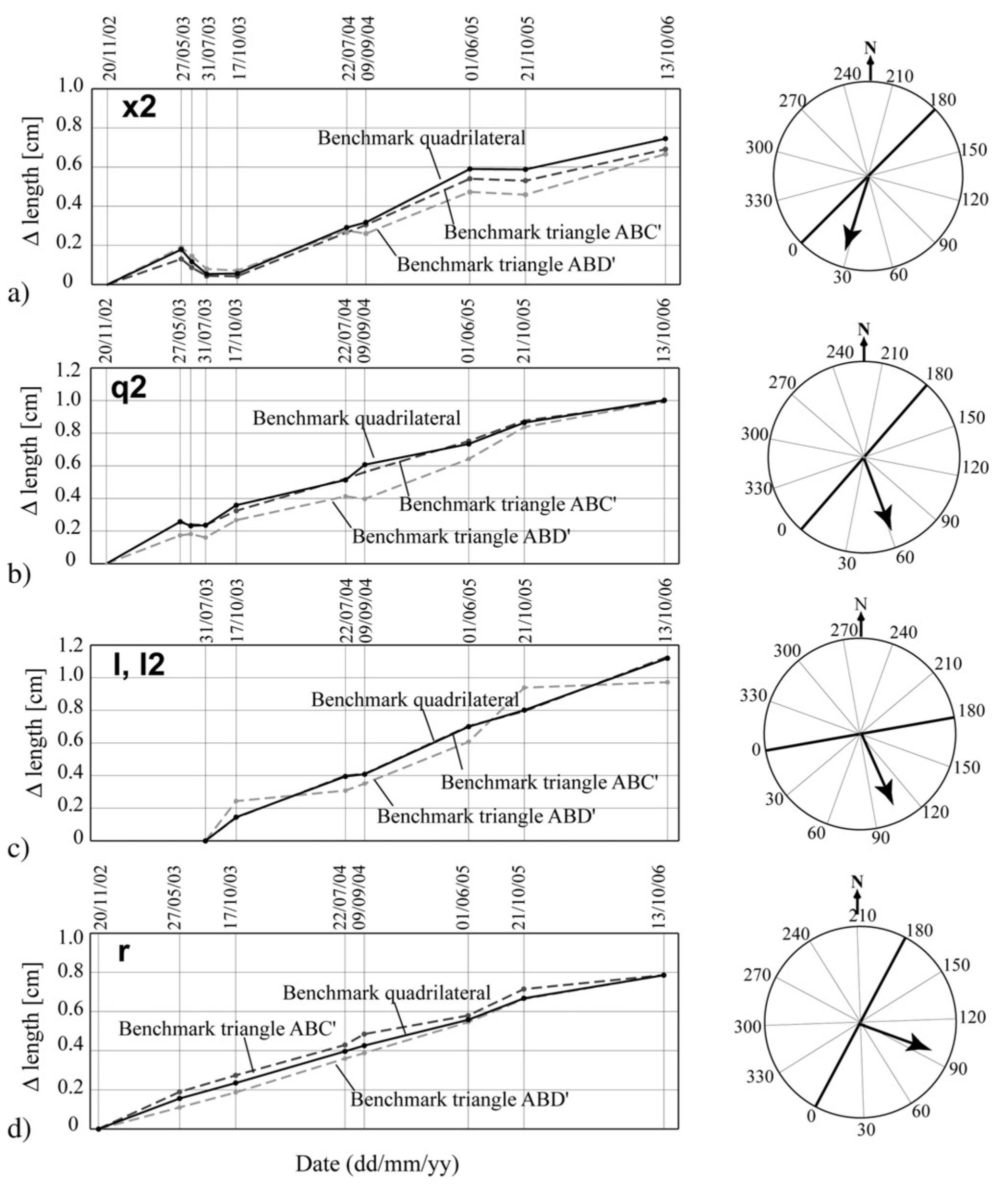

Fig. 6. Estimates of relative displacement magnitude and azimuth across active faults obtained from quadrilateral arrays. The results obtained by the grid search approach for all linear strains in the quadrilateral are plotted with a solid line, and those obtained by Baum et al.'s (1988) separate triangles approach are denoted by the dashed lines. Also shown is the azimuth of the horizontal displacement vector of the south side of the fault with respect to the north side. The bold line denotes the strike of the faults. Results are for: a) fault *x2*, b) fault *q2*, c) fault *l*/*l2* and d) fault *r*.

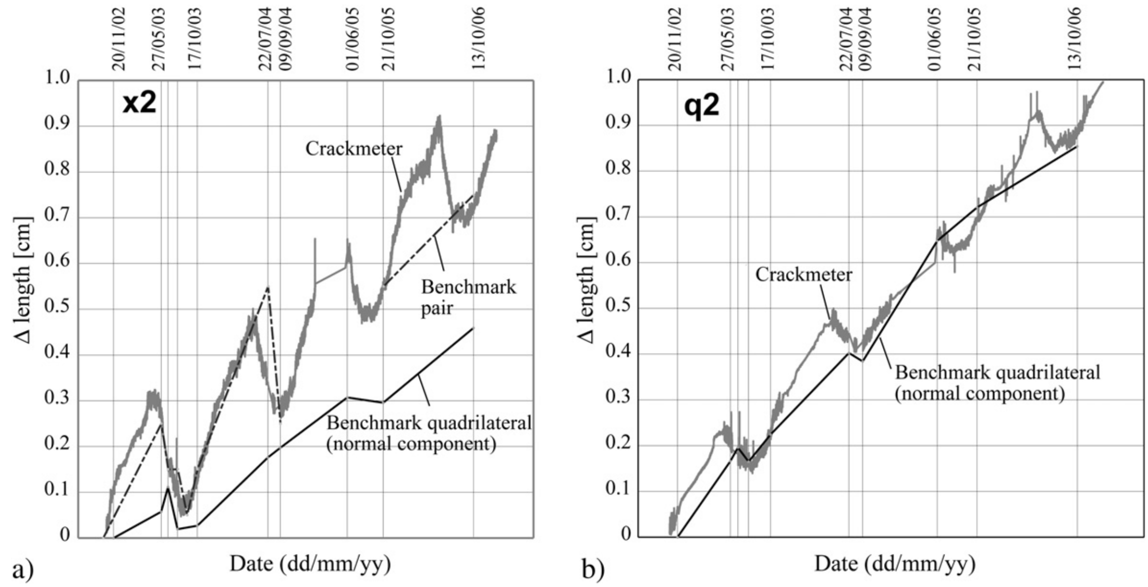

Fig. 7. Comparison of relative displacement estimates across faults (a) x2 and (b) q2, obtained from the quadrilateral arrays, simple benchmark pairs and crackmeters. The black solid lines show the normal component of the horizontal displacement vector obtained by the grid search method. a) Measurements across fault x2: the crackmeter and simple benchmark pair are co-located, whereas the benchmark quadrilateral is several meters away. b) Measurements across fault q2: the crackmeter and benchmark quadrilateral are co-located.

geometry logs indicated that all boreholes deviated from vertical below 20 m (Fig. 8). The deviation reached 14° at the bottom of SB 120 and 8° in SB 50N and SB 50S, and was consistently oriented towards the E–SE, which is approximately perpendicular to the foliation. Thus, the borehole trajectories were drawn towards the normal to the foliation plane. PVC grooved-inclinometer casing was cemented in all three boreholes. In accord with standard practice, the groove-pair chosen as the *A*-axis was oriented during installation so as to lie in the direction of expected maximum displacement, which is N165°E in SB 120, N140°E in SB 50S and N160°E in SB 50N (Fig. 9c). The casing of SB 120 was also fitted with external brass rings at 1 m intervals for surveying with an induction coil transducer extensometer system (Interfels 'Increx' system).

The initial Increx and inclinometer surveys were performed 10–12 days after cementing the casings in autumn 2001. Following standard procedures (see Dunnicliff, 1988), a torsion survey was

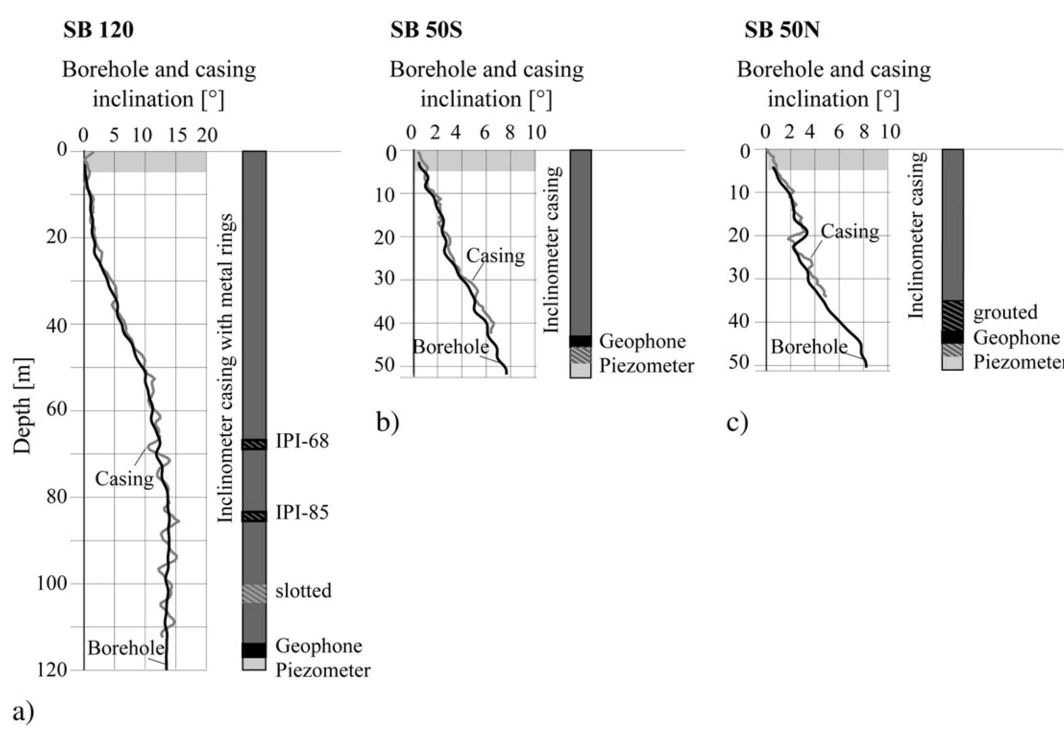

Fig. 8. Borehole inclination and instrumentation completion for (a) SB 120, (b) SB 50S and (c) SB 50N. The inclination of the borehole was measured after drilling using both a borehole geometry probe and an optical televiewer. The inclination of the casing is shown by the grey line, and was derived from the initial inclinometer survey. Here the buckling of the casing in SB 120 is evident.

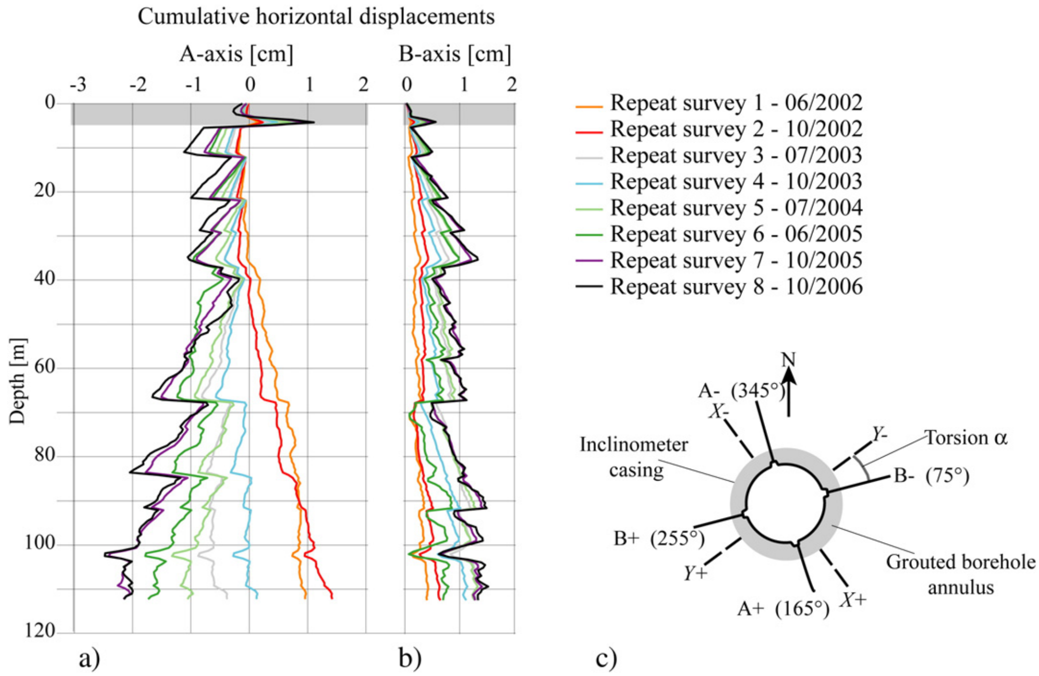

Fig. 9. Cumulative horizontal displacement profiles for the first 8 repeat surveys of SB 120 after applying the depth-matching procedure and the empirical torsion correction (Table 2). The profiles were obtained by integrating the incremental horizontal displacements from the top downwards. Shown are the horizontal displacement components in the a) *A*-axis direction and b) *B*-axis direction. c) Coordinate conventions used in the inclinometer measurements. The view is from above. The *A*–*B* axis pair denotes the groove orientations at the surface, and the *X*–*Y* pair is the groove orientation at depth.

conducted to determine the groove orientations at depth. The inclinometer and Increx repeat surveys that followed were performed twice a year in spring and autumn. The surveys could be performed to a depth of 112 m in SB 120, 42.5 m in SB 50S and 34.3 m in SB 50N.

All inclinometer surveys were conducted with the same 61 cm base length, bi-axial instrument manufactured by the Slope Indicator Company, following standard procedures (Mikkelsen and Wilson, 1983; Dunnicliff, 1988). The difference between a repeat and the initial survey gives the profile of inclination change along the borehole. The random error of the inclinometer survey is typically less than 0.16 mm/interval (Mikkelsen, 2003; Moormann, 2003) and includes limitations in the precision of the sensor and the influence of environmental factors (Dunnicliff, 1988). Systematic errors have multiple sources and are much more important than the random errors for inclinometer surveys because they are always in the same sense and thus accumulate. Mikkelsen (2003) showed that systematic errors can increase drastically if the casing deviates from vertical by more than several degrees. For the present data, the reduction of systematic errors was vital because the signals being resolved were relatively small. The corrections we devised and applied to the data, some of them novel, are described in detail in the Appendix. To summarize here, first a depth-matching procedure was applied to eliminate systematic errors arising from axial strains along the casing due to rock mass deformation and/or from differing stretches of the cable used to lower the inclinometer probe. Then an 'empirical torsion correction' was required to address limitations of the standard torsion correction procedure as described in Dunnicliff (1988), arising due to non-vertical, contorted casings. This involved an iterative procedure to find the torsion profile which, when applied to the initial inclinometer survey, yielded a trajectory that was in accord with that estimated from the fully-oriented geophysical borehole logs. The difference in the measured and corrected torsion profiles is believed to be related to buckling of the 71 mm diameter casing in the 150 mm diameter borehole which produced a more complicated 3-D variation in groove orientation along the casing than could be corrected by the standard procedure.

In this paper, we chose to express horizontal displacements as displacements at the end of the inclinometer probe with respect to (wrt) its top and to integrate from the top downwards, rather than vice versa, as per the usual convention. This was necessary because it could not be established that the bottoms of the boreholes were founded in stable rock. Only for integration with the geodetic displacement data, we integrate from the bottom upwards to facilitate comparison with the absolute horizontal displacement vector of the borehole top from the geodetic survey.

The Increx extensometer surveys in SB 120 were performed using a 2 m long probe without guiding wheels following standard procedures (Dunnicliff, 1988). The vertical component of incremental displacement was obtained from the measured value by multiplying by the cosine of the borehole dip. Note that the 'horizontal incremental displacements' obtained from the inclinometer measurements are already referenced to a horizontal plane by the standard processing conventions and thus require no correction for borehole inclination.

Two vibrating-wire, bi-axial in-place inclinometers with a 2-m base length were deployed across active fractures in SB 120 to continuously monitor inclination changes and thus determine the

Table 2
Depth offsets at the bottom of the repeat surveys which yield the best depth-match with the initial survey

Repeat survey	Date	SB 120 maximum depth offset [cm]	SB 50S maximum depth offset [cm]	SB 50N maximum depth offset [cm]
1	06/2002	−2	0	−1
2	10/2002	−2	0	−2
3	07/2003	−1	0	−2
4	10/2003	−1	0	−1
5	07/2004	−3	0	−2
6	06/2005	0	0	−4
7	10/2005	0	0	−3
8	10/2006	0	0	−3

The mismatch is assumed to increase linearly along the profile from zero at the surface.

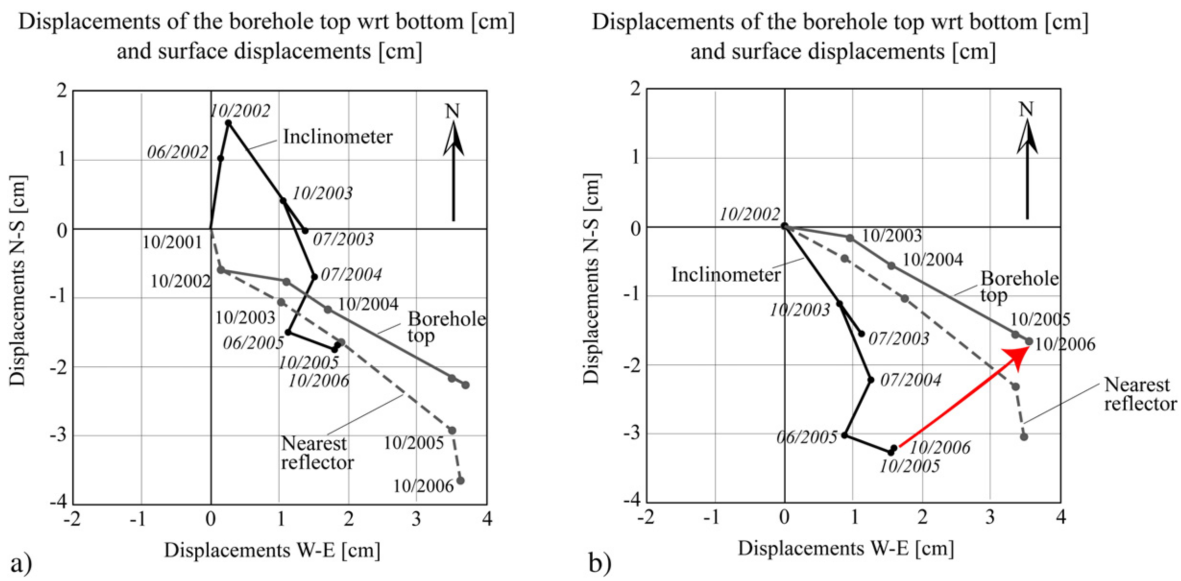

Fig. 10. a) Horizontal movement of the top of the borehole with respect to the bottom obtained from upward integration of the inclinometer profiles since the initial survey in 2001. The grey-dashed line denotes the absolute movement of reflector 007, which lies some 20 m to the SSE of SB 120. The solid-grey denotes the movement of the borehole top itself which was included in the geodetic surveys in 2002. b) Same as a) but with the first year of data excluded. The arrow denotes the implied absolute displacement of the casing bottom at 115 m, but is not considered reliable.

temporal characteristics of fracture slip. The instruments were removed during repeat surveys of the inclinometer casing and repositioned afterwards. Unfortunately, the original instruments were found to suffer from drift and spurious offsets, as has since been recognised in laboratory tests (LaFonta and Beth, 2001) and in other field studies (Simeoni and Mongiovi, 2003). In December 2003, the defective instruments were replaced with two redesigned models. These were positioned across active fractures at 84.5 and 68.0 m depth but only the latter installation proved stable. The instruments were sampled every 6 min together with the piezometer and the data recorded on a Campbell Scientific CR10x data logger.

6.2. Cumulative horizontal displacement profiles for SB 120

A total of eight repeat inclinometer and INCREX surveys were conducted in each of the deep boreholes between 2002 and 2006. The resulting cumulative horizontal displacement profiles for SB 120 are shown in Fig. 9. Numerous steps in the displacement profiles are evident which progressively increase with time, indicating on-going displacements across discontinuities that intersect the borehole. These steps are separated by intervals with constant slopes which change with time, indicative of rotating rigid blocks.

However, the evolution of the displacements along these intervals, and indeed the overall slope of the depth-trends of the profiles are somewhat irregular, particularly during the first two surveys. For example, the direction of the *A*-axis displacement accrued from the initial survey at the time of repeat surveys 1 and 2 reverses by the time of survey 3, and then reverses again, resulting in zero net displacement at the time of survey 4. The effect of the reversals is seen most clearly in the plot of the displacement path of the borehole top with respect to the bottom shown in Fig. 10a. The inclinometer data suggests the borehole top moved towards the north wrt the bottom during the first year, which is in the opposite direction to the absolute displacement of the top during this period, a result that is improbable. In the subsequent 4 years, the direction of the two paths is in reasonable accord (Fig. 10b). In the Appendix we show that the erratic variation of the evolution of the inclinometer profiles most probably reflects the presence of 'sensor-rotation error'. This systematic error is small for vertical casing but grows with increasing casing deviation from vertical (Mikkelsen, 2003), which explains why the erratic behaviour is seen in SB 120 below 35 m. For further analysis we assume that sensor-rotation error dominates the profile evolution during the first year and true movement dominates in subsequent years, albeit with a component of error. Thus, we exclude the first year of data and consider the period 10/02–10/06. For this period, the difference between the displacements of the borehole top derived from inclinometer and geodetic data is 2.5 cm towards ENE as shown in Fig. 10b. Given the unknown component of error present in the profiles, we consider it probable that some displacement occurs below the borehole bottom, but the magnitude and orientation of it is uncertain.

The uncertainty of the degree of error affecting the inclination profiles below 35 m also impacts the estimates of the rotation rates of the rigid blocks. Although the rates are not precisely resolved, it is clear that rotation is occurring in the sense that the tops of the blocks move to the southeast with respect to their bottoms (Fig. 9a,b). An identical sense of movement is seen above 35 m, where the profile evolution is regular and the rotation rate is quantitatively resolved.

6.3. Incremental displacement across discontinuities at depth

Incremental horizontal displacements derived from the inclinometer surveys, unlike cumulative displacement, are not strongly affected by systematic errors. The profile of incremental horizontal displacement accrued in SB 120 between the initial and eighth survey is shown in Fig. 11a. Eleven peaks are evident, all of which coincide with faults or fracture zones identified on the optical televiewer log (Fig. 11d). The peaks indicate that horizontal components of displacement of as much as 1 cm occurred on those discontinuities, which hereafter will be referred to as 'active faults'. Most displacement zones are contained within one measurement interval, indicating that the deformation is highly localised. However, several extend over more than one interval, reflecting movement across broad zones defined by the intersection of steep active faults, or wide fracture zones. Two anomalies are noted, at 5 and 102 m depth, consisting of adjacent positive and negative peaks. The first of these is likely related to the stiffness contrast marking the end of the borehole collar (a cemented steel stand-pipe), which ends at 5 m depth. The second anomaly coincides with a slotted open hole piezometer interval (positioned between 100 and 105 m), for which the absence of grout enables the casing to freely deform (possibly buckling). The active faults coincide for the most part with members of the NW-dipping fault set F2, the extensions of faults 120_10 and 120_16 being traceable on georadar images out to 30 and 85 m respectively from the borehole (Spillmann et al., 2007b).

The profile of incremental axial strain for the eighth repeat survey is shown in Fig. 11b. A positive value indicates extension. Since the base length of the inclinometer and Increx measurements differ, the 1.0 m sampled Increx profiles were interpolated and re-sampled at 61 cm. Almost all peaks indicate interval shortening and coincide with active faults. With one exception, the implied vertical component of displacement was less than the horizontal component. The two components were combined to obtain the magnitude and orientation of the relative displacement across the active faults, the values of which are indicated in Fig. 11c and listed

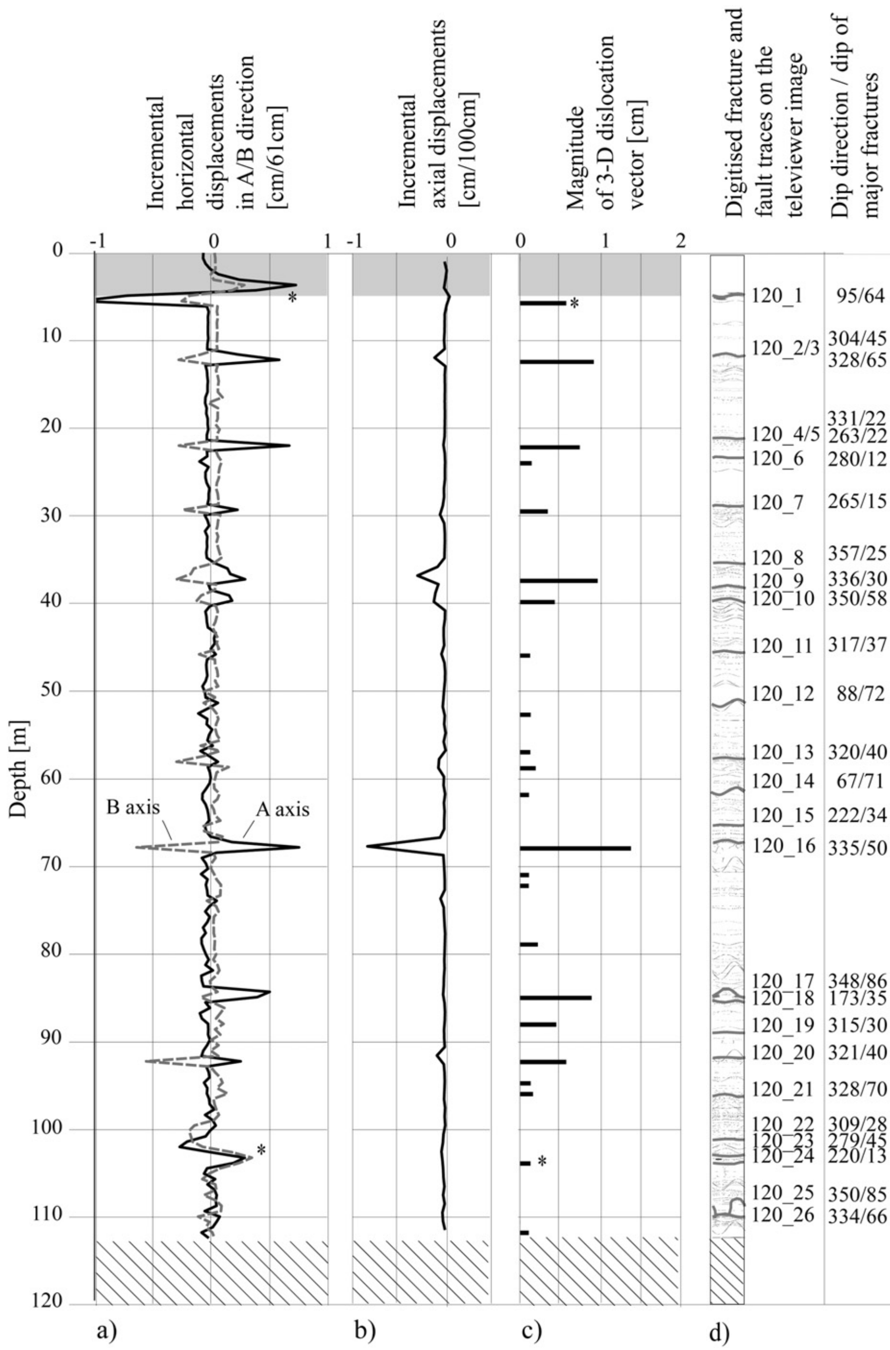

Fig. 11. Comparison of the 3-D displacement data from the eighth repeat survey in October 2006 of SB 120 with geological data from the optical televiewer images. a) Incremental horizontal displacements per inclinometer interval (61 cm). The *A*–*B* axis pair is oriented such that the *A*–axis coincides with the expected direction of maximum signal. Asterisks denote ungrouted casing sections. b) Incremental axial displacements interpolated to intervals of 61 cm. c) Magnitude of the 3-D dislocation vectors across localised displacement zones. d) Fracture traces from the optical televiewer images. Major fractures are highlighted with the dip direction and dip given.

Table 3
Inferred dislocation, accrued over 5 years, of active faults in SB 120 for which the rate exceeds 0.5 mm/year

Depth of dislocation zone		Dip-direction and dip of active fracture	Azimuth, dip and magnitude of 3-D dislocation vector (bottom block wrt to upper)		Fault characteristics on televiewer image	Maximum shear component in plane of the fracture	Normal component of dislocation normal to the fracture
[m]		[°/°]	[°/°]	[cm]		[cm]	[cm]
12.3	120_3	328/65	139/−6	0.90	Open, with fine infilling	0.48	0.76
22.1	120_4	331/22	142/0	0.72	Schistous, rotated blasts	0.67	0.26
29.4	120_7	265/15	117/−4	0.34	Dark (mica rich) section	0.33	0.05
37.3	120_9	336/30	118/−23	0.94	Phyllonite	0.94	0.02
39.8	120_10	350/58	129/−21	0.42	With fine infilling	0.39	0.18
67.8	120_16	335/50	132/−36	1.34	Densely foliated and fractured zone, fine infilling	1.32	0.26
84.9	120_17	348/86	162/−1	0.87	Densely foliated and fractured zone	0.14	0.86
89.1	120_19	315/30	291/2	0.44	Phyllonite	0.40	0.19
92.2	120_20	321/40	89/−8	0.56	Densely foliated and fractured zone	0.54	0.16

The vector orientation denotes the displacement of the footwall with respect to the hanging wall and dips are positive downwards. The maximum shear and normal components of dislocation were computed from the given orientation of the associated fault which in almost all cases dips to the NW. Most active faults have predominant shear components with the hanging wall moving down-dip with respect to the footwall. The exception is the sub-vertical fault 120_17 which has a predominant opening-mode component.

in Table 3. In cases where the displacement was distributed across several adjacent intervals, the dislocation vector was summed across all points where the displacement magnitude exceeds a threshold of 0.5 mm. Dislocation magnitudes for the 5 year period are typically several millimeters with a maximum of 13 mm at fault 120_16. The direction of displacement of the footwall wrt the hanging wall is predominantly towards the SE, with values ranging between 110° and 160°. Since almost all active faults dip to the NW, this means they are activated as normal faults with varying normal components of dislocation (Table 3). The normal and shear components of the dislocations resolved across the plane of the faults are listed in Table 3 for fractures with dislocation rates >0.5 mm/year.

The corresponding results for the surveys in SB 50N and SB 50S are shown in Fig. 12 and listed in Table 4. Since the casings in these boreholes were not equipped for Increx extensometer surveys, only horizontal displacements can be estimated. Again, several faults are seen to be undergoing relative displacements. In SB 50S, two zones of distributed displacements are evident which coincide with groups of fault traces. The uppermost of these, which includes the faults 50S_3 to 50S_6 (Fig. 12c), is too complex to associate dislocations to specific faults. The complexity of this zone may be due to the presence of a long sub-vertical fault trace, or the absence of grout at a zone where borehole spalling has occurred at the faults or fracture zones. For SB 50N, only one peak in incremental horizontal displacement is present (at 21 m depth; Fig. 12d), which correlates with the location of a steep, open fault (50N_2; Fig. 12f).

6.4. Evolution of displacements across active faults and fracture zones

The evolution of the long-term magnitude of cumulative horizontal displacement across selected active faults is shown in Fig. 13a. In most cases, the measured displacement rates are essentially constant with only small variations. A comparison of the horizontal component of the displacement vector derived from the inclinometer surveys and the in-place inclinometer at 68 m depth is shown in Fig. 13b. The magnitude and direction of the two displacement vectors agree to within the expected error. The continuous record of displacement from the in-place inclinometer clearly reveals an annual periodicity, with displacement rates reaching a minimum in the late summer months.

7. Discussion

7.1. Active faults and fracture zones

The surface and borehole displacement measurements support the inference from geological mapping that the displacement field is complex and localised across active faults and fracture zones within the rock mass. Fig. 14 presents two approximately SE–NW vertical cross sections along the profiles indicated in Fig. 4, which pass through SB 120 (A–A') and SB 50S/SB 50N (B–B'). The cumulative PDFs of microseismic event locations on the section surfaces are shown as background, and the subset of faults that are active is indicated by the solid lines. The F-2 fault 120_16 is the most prominent active structure imaged in the boreholes with an average displacement rate of 2.6 mm/year. This fault could be traced more than 85 m with borehole radar to its outcrop as surface fault Z6 (Spillmann et al., 2007b). However, it is for the most part aseismic, with at most having weak activity near its intersection with the borehole. In fact, many of the active faults appear to be aseismic, and for those that are seismogenic, the microseismicity tends to be localised in patches on the fault plane. This might be taken to suggest a focussing of activity at locations on the fault plane where movement is impeded by some geometric irregularity such as a rock bridge, although other explanations are possible. For the zone of highest microseismic activity, i.e. close to the rockslide scarp, a high degree of internal fracturing of the rock mass can be inferred.

7.2. Extent of the unstable rock mass

The limited coverage of the geodetic network produces some uncertainty in the extent of the unstable rock mass. To the northwest, the boundary was taken as Z10 in Fig. 3, which was the most northerly fault measured to be actively opening. This fault lies some 10–15 m to the north of SB 50N, whose wellhead geodetic measurements indicate to be moving ESE at a rate of 5.5 mm/year (Fig. 3). A benchmark pair and crackmeter across Z10 indicated an average opening rate of 2 mm/year (Fig. 7) whilst a benchmark quadrilateral located several metres along strike indicated a rate of 1 mm/year with a marked right-lateral shear component (Fig. 3). These data thus suggest that the limit of the unstable mass actually lies further to the NW, possibly at Z2b or Z11, both of which were associated with minor microseismic emissions

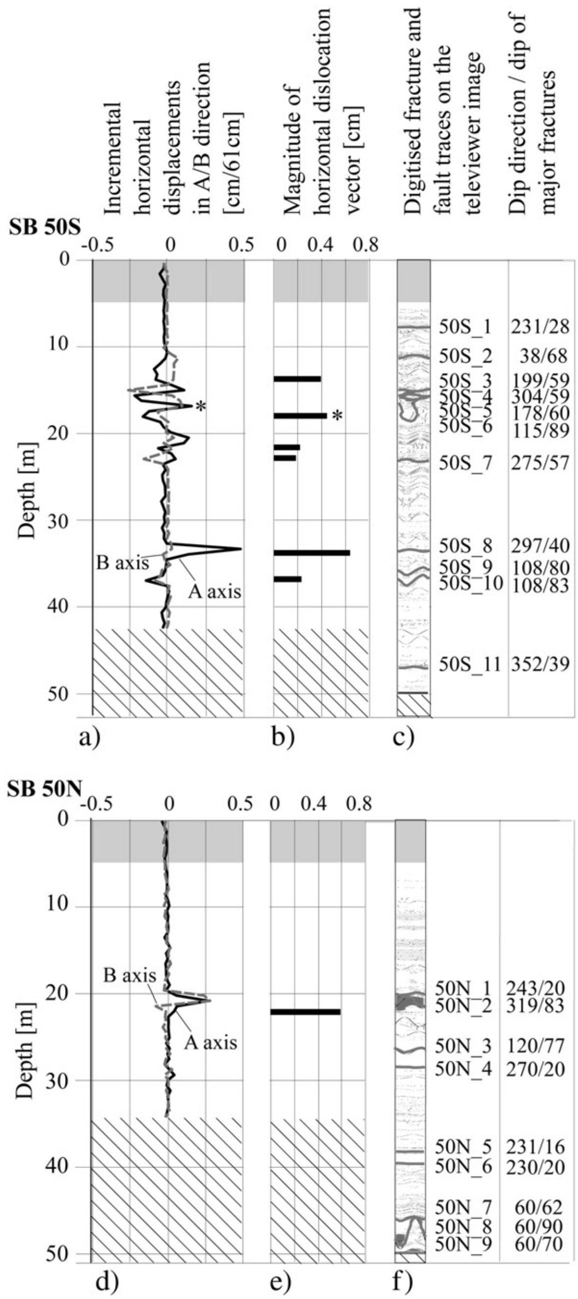

Fig. 12. Comparison of the incremental displacements from the eighth repeat inclinometer survey of SB 50S and SB 50N (Oct. 06) with geological data from the optical televiewer images. Respectively, a), d) Incremental horizontal displacements per inclinometer interval (61 cm). b, e) Magnitude of the horizontal dislocation vectors across localised displacement zones. c, f) Fracture traces from the optical televiewer images. Major fractures are highlighted and the dip direction and dip given.

(Fig. 14), although no evidence of opening was visible at the surface (here the rock surface is covered with colluvium).

To the west, the boundary was assumed to be coincident with the faults/fracture zones Z2a and Z2b, largely on the basis of the fault morphology. Heincke et al. (2006b) located a zone of very low seismic velocities to the west of these faults, but whether the unstable area extends to this area could not be resolved due to the absence of geodetic reflectors. Likewise, the boundary to the SE could not be constrained by geodetic or borehole measurements since it lies on the inaccessible scarp. The uppermost 50 m of the scarp is characterised by a band of intense microseismicity (Fig. 14). No prominent faults or lineaments are seen on the scarp face at the limit of the microseismicity, although the limit might be due to limitations in the sensor array and/or velocity model rather than an absence of activity. Currently-unpublished results (pers. communication H. Raetzo, 2007) of ground-based DINSAR surveys of the 1991 scarp face performed since 2005 from an instrument positioned on the opposite side of the valley close to the geodetic survey station (Fig. 2) indicate along-line-of-sight velocities for this microseismic zone of up to 14 mm/year (Fig. 14). Decreasing active displacement extends significantly down the scarp, beyond the SE limit of the microseismic zone, probably to the failure surface of the first 1991 rockslide (Fig. 2 of Part 1). This supports the absence of a single sliding surface at the base of the unstable mass.

7.3. Measured block kinematics

The pattern of deformation of the rock mass observed in SB 120 is dominated by “normal-fault” movement of active F-2 faults dipping predominantly to the NW, the rock between these faults rotating as rigid blocks such that their tops move towards the SE (i.e. towards the valley) wrt their bottoms (Fig. 9). This is illustrated in Fig. 14, where arrows marking the intersection of the borehole with the active faults indicate the relative displacement-rate vectors of the footwalls wrt the hanging walls. As the relative displacement direction in most cases is oriented within 30° of the fault dip directions (Table 3), the displacements are sensibly represented on the 2-D projections. This, together with the sense of block rotations, indicates toppling movement as an important component of the kinematics in the current instability.

Fig. 15 shows a strongly simplified kinematic model illustrating idealized relationships between fault movements and block rotations in the study area. As the NW-dipping F-2 faults are reactivated as planar persistent faults, the foliation parallel F-1 faults can be activated as second-order en-echelon structures, such as conjugate Riedel shears (e.g. Hancock, 1985). This model is very close to what can be seen for faults 120_4 and 120_7 (Fig. 14). The intersection of F-2 faults with steeply SE dipping F-3 faults, both reactivated as normal faults, will additionally create graben structures, typical for extensional domains behind outward rotating blocks. These are visible in the geomorphology at the study site.

A deviation from the toppling pattern occurs towards the bottom of SB 120 where the block below an active group of fractures at 104 m (120-23/24) does not rotate significantly (Fig. 9). Since this is the lowermost block sampled, the significance of this change is unclear. It should also be noted that a sub-vertical fault 120_17 at 84 m depth is activated in predominantly opening mode rather than shear, which is not consistent with a simple toppling model controlled by planar F-2 faults.

7.4. Kinematic model

The style of deformation defined by the collective measurements constitutes the foundation for identifying the rock slope instability processes acting at Randa. In comparison to the strongly simplified kinematic model shown in Fig. 15, the scatter of F-2 fault orientations is considerable (see Fig. 8 of Part I) and the fault pattern is three dimensional. Accordingly, the complexity of the displacement field and the heterogeneous lithological structure does not allow identification of a simple kinematic instability model. Traditional flexural or block-flexural toppling models (e.g. Goodman and Bray, 1976; Nichol et al., 2002) that can account for both the observed normal-faulting shear displacements and the opening of sub-vertical faults at depth, require densely-spaced discontinuity sets dipping steeply into the slope and cross-cutting discontinuities dipping gently out of the slope. At the Randa site, however, the F-1 and F-2 sets of faults and fracture zones that dip into the slope have a spacing of several tens of meters, and large fractures that dip out of the slope are almost absent.

Table 4
Characteristics of faults associated with dislocation zones in SB 50S and SB 50N together with the magnitude and azimuth of the relative displacement vector developed over the 5 year monitoring period

Depth of dislocation zone		Orientation of active fracture	Azimuth and magnitude of the horizontal dislocation vector (movement of bottom block wrt to top)		Characteristics on televiewer image
[m]		[°/°]	[°/°]	[cm]	
SB 50S					
13.9	50S_2	38/68	281	0.37	Open, silt coated
34	50S_8	297/40	140	0.56	Densely fractured zone
SB 50N					
20.9	50N_2	319/83	205	0.57	Open

Only the horizontal component of the relative displacement vector could be estimated due to the absence of extensometer readings for these two boreholes.

Instead, the heterogeneity of the measured displacement field typifies that commonly observed in many massive crystalline rock slopes where no systematic set of closely spaced or highly persistent structural controls are present. Hungr and Evans (2004) describe the associated kinematic model as a rock slope 'collapse', for which the instability is partly controlled by the brittle destruction of rock bridges separating a more dispersed set of discontinuities of limited persistence in stronger rock. This has been explored numerically by Eberhardt et al. (2004) for the earlier 1991 Randa rockslide. In the upper slope, the removal of lateral confinement created by the scarp of the 1991 slide together with the F-2 faults could combine to enable flexural block toppling (Fig. 15). Locally, the 3-D block movements would be controlled by neighbouring and intersecting fault sets.

Below this, increasing stresses with depth combined with extensional downslope strains may be promoting a more complex deformation mode involving rock mass yield and brittle fracture together with slip, movement and opening along existing structures, which may combine to produce a small outward rotational/translational component of deformation. However, these cannot be confirmed as they extend below the rock volume sampled by the 120-m deep borehole (i.e. 2200 masl). The unintentional deviation of the borehole from vertical greatly degraded the resolution of cumulative horizontal displacements from the inclinometer data, such that it was not possible to determine the amount of displacement that occurs below 115 m with certainty.

Willenberg (2004) did perform some simple 2-D distinct-element modelling to explore how the block movements may evolve as a function of different kinematic models related to differently oriented fractures with limited persistence and these have shown enough promise that a detailed 3-D numerical modelling study has been initiated. This work will see the use of DINSAR data to help constrain the displacements below those intervals monitored by the deep inclinometers.

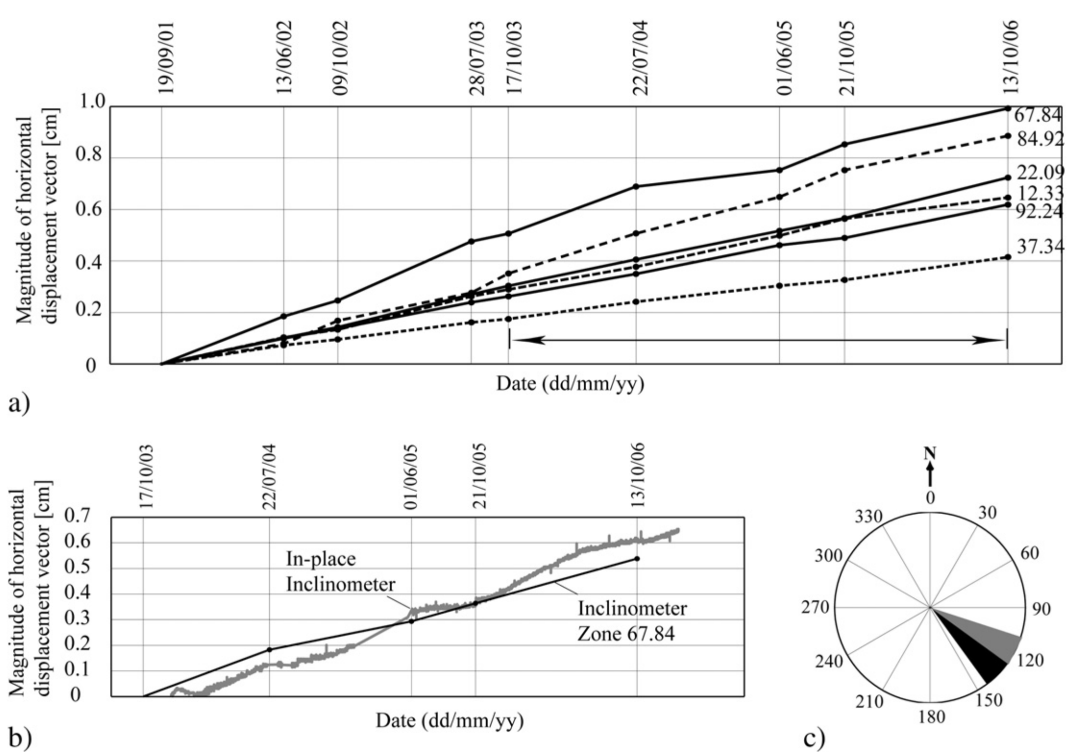

Fig. 13. a) Evolution of the magnitude of horizontal incremental displacement across a selection of active faults in SB 120 as derived from the inclinometer measurements. The displacement rates are essentially constant with a slight seasonal perturbation present in some cases. b) Comparison of the histories of horizontal incremental displacement magnitudes derived for the in-place inclinometer at 68 m depth and the corresponding inclinometer intervals. c) Range of azimuths of the horizontal incremental displacements shown in (b) for the in-place inclinometer (light grey area) and periodic surveys (dark grey area).

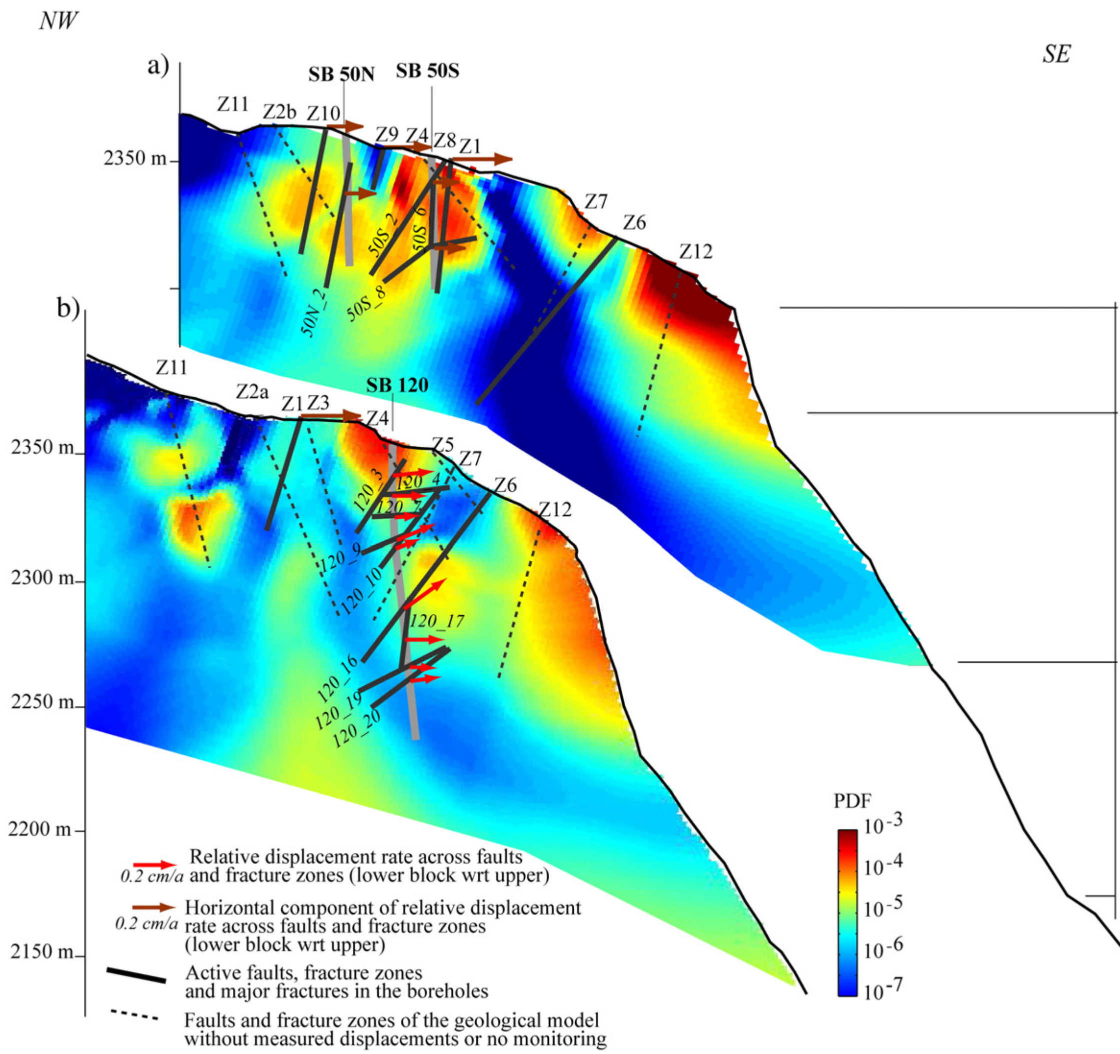

Fig. 14. Vertical cross sections through the study area (see A–A' and B–B' in Fig. 4) showing the cumulative PDF of hypocenter locations as background. The borehole trajectories are shown in grey. Active faults that intersect the surface or the boreholes are shown by solid lines, whereas the dashed lines denote faults where no on-going dislocation was detected. Line-lengths denote the minimum along-dip extension of the faults inferred from borehole geophysical surveys. The designation IDs of the faults that intersect the surface are indicated. The colored arrows denote the relative displacement vectors across the active faults, the arrow indicating the movement of the lower block with respect to the upper. For the two 50 m boreholes the inclination of the borehole displacement vectors is unknown. The provisional results of ground-based DINSAR surveys of the scarp are shown at right for section A–A'. The values are displacements along the line of sight accrued over 1 year.

7.5. Seasonal variations

All continuous displacement measurements indicate an annual variation in rock mass deformation. The variations seen on the crackmeter records most likely reflect shallow thermo-elastic strains, although the presence of a component reflecting deep-seated rock mass deformation is possible. The in-place inclinometers indicate a marked reduction in displacement rate during the late summer months, which cannot be explained by thermo-elastic effects alone. Comparable seasonal variations of displacements on unstable rock slopes have also been reported by Krähenbühl (2004) and Watson et al. (2004). These are attributed to complex interactions of climatic factors, groundwater flow, thermo-elastic strains and the geological structure of the slope (Watson et al., 2004). However, the discontinuous and seasonal effects that influence the measured pore pressure response at Randa, further complicated by the presence of perched water tables and a non-systematic network of fractures controlling flow, make reliable measure of variations of the contiguous water table tenuous at best.

8. Conclusions

The surface and borehole displacement measurements at the study area confirmed the expectation from geological mapping (Part I) that the displacement field within the rock mass is complex. Rock mass deformation for the slope is clearly accommodated along faults and fracture zone networks. The slide body was seen to be composed of blocks with dimensions of several tens of meters, compartmentalized along 3 sets of faults with trace lengths of up to a few hundreds of meters. Near the front of the scarp to the SE, the geodetically-determined surface displacements in large part reflect toppling of the blocks. This toppling is accommodated largely through normal-fault movement on NW-dipping faults bounding rigid blocks that undergo rotation such that their tops move towards the valley. As the dispersion of the fault orientations is large and the 3 faults sets are not orthogonal, the block movements are complex and three dimensional in nature. The absence of a clear set of highly persistent, closely spaced systematic structural controls (confirmed in Part I) suggests that elements of rock mass yield and brittle

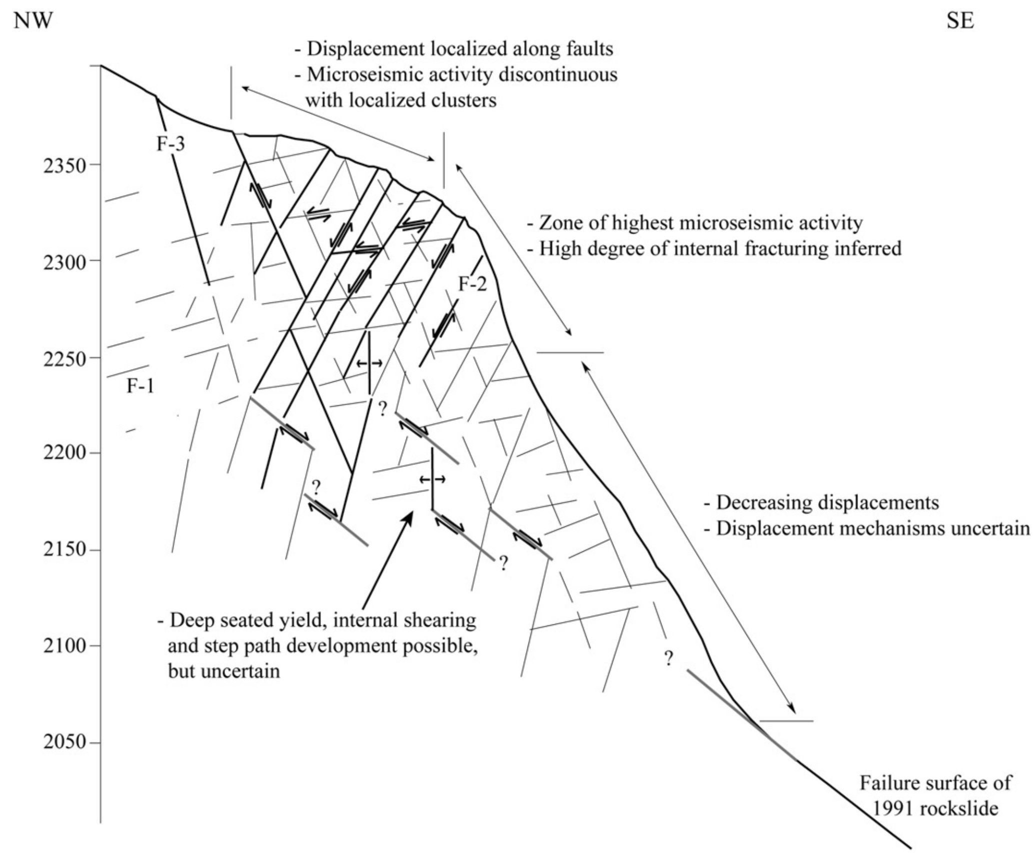

Fig. 15. Simplified 2-D kinematic model based on a schematic cross-section through the rock mass along a NW–SE profile showing the three fault and fracture zone families, their persistence and relative displacement directions.

fracture together with slip, movement and opening along existing structures may also play a contributing role in the kinematics of the instability.

Shear displacement rates on the faults intersecting the holes of up to 5 mm/year were resolved. Year-averaged relative displacements across surface fractures were relatively constant, with opening rates of up to 4 mm/year.

Significant microseismic activity was also detected, accompanying the slope deformation. The microseismicity tends to be localised in patches on active faults. This might be taken to suggest a focussing of activity at locations on the fault plane where movement is impeded by rock bridges. Conversely, some active faults appear to be aseismic.

The methodology presented here to contend with the complexity and heterogeneity observed at Randa emphasizes the need for an integrated approach, together with an overarching understanding of the instability mechanism. The multi-disciplinary study presented here and in Part I is probably more detailed than could be contemplated for adoption as a standard hazard assessment procedure, although elements of it are probably indispensable for obtaining an adequate understanding of the internal 3-D kinematics of a complex rock slope hazard.

Acknowledgements

The authors would like to acknowledge the contributions of Prof. Alan Green, Prof. Hansruedi Maurer, and Dr. Björn Heincke (now NGU, Trondheim) of the Institute of Geophysics, ETH Zürich. The geodetic surveys are conducted and analysed by the company Klaus Aufdenblatten of Zermatt. The digital terrain model was provided by the Centre de Recherché sur l'Environment Alpin (CREALP). The boreholes were drilled by the Arge ISR Injectobohr SA & SIF Groutbor SA. The geotechnical and borehole monitoring system was installed by Stump Foratec AG who also performed the inclinometer/extensometer surveys. Optical televiewer logs were run by Terratec GmbH, Heitersheim. Germany. This project was financed by the Swiss National Science Foundation (Project No. 2100-059238.99).

Appendix A.

A.1. Empirical torsion correction

In deep boreholes such as SB 120 it is common for inclinometer casing to twist in torsion so that the orientation of the grooves and hence the axes of the two inclination measurements changes with depth. Knowledge of the profile of groove orientation is essential to allow the measurements at depth (referenced to local groove coordinates *X* and *Y* in Fig. 9c) to be expressed in the coordinate system defined by the groove orientation at the surface (*A*- and *B*-axes in Fig. 9c). A 1.5 m long 'torsion survey' probe was employed to measure the difference in the azimuthal direction of the upper and lower wheel-pair to a precision of 0.1°. From these data, the profile of groove orientation with respect to the *A*- and *B*-axes is obtained by integration from the top, a procedure that results in increasing error with depth (Fig. A-1b). The resulting profiles for the three boreholes were used to reduce the initial inclinometer surveys to geographic coordinates and thus obtain the trajectories of the casings. Comparison of the casing trajectory for SB 120 obtained in this manner with the borehole trajectory obtained from both borehole geometry and optical televiewer logs showed a major discrepancy below 40 m

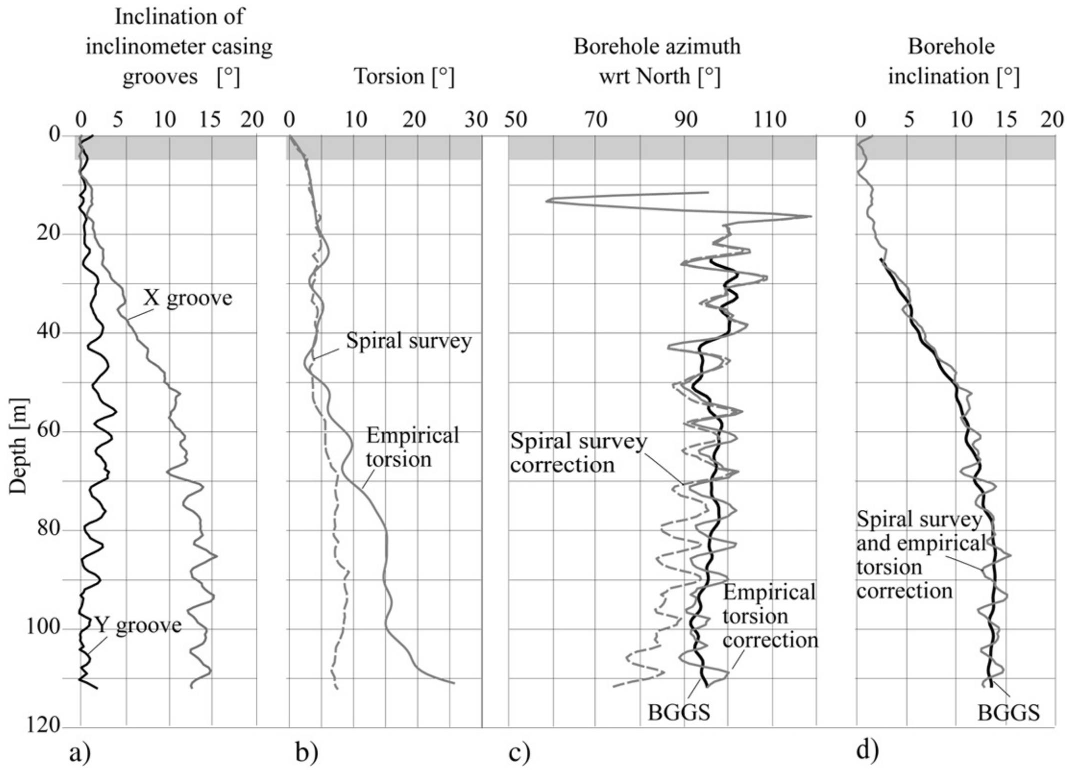

Fig. A-1. a) Raw inclination data (*X* and *Y*-grooves) of the initial survey in SB 120 expressed in degrees from vertical. b) Torsion profile measured with the spiral probe (dotted) and the empirically derived torsion (solid). c) Azimuth and d) inclination of the SB 120 casing trajectory derived from the inclinometer data using both the spiral-survey and the empirical approach, together with the true borehole trajectory from the borehole geometry log (BGGS). The periodic fluctuations in the casing trajectory reflect buckling of the casing within the 150 mm hole.

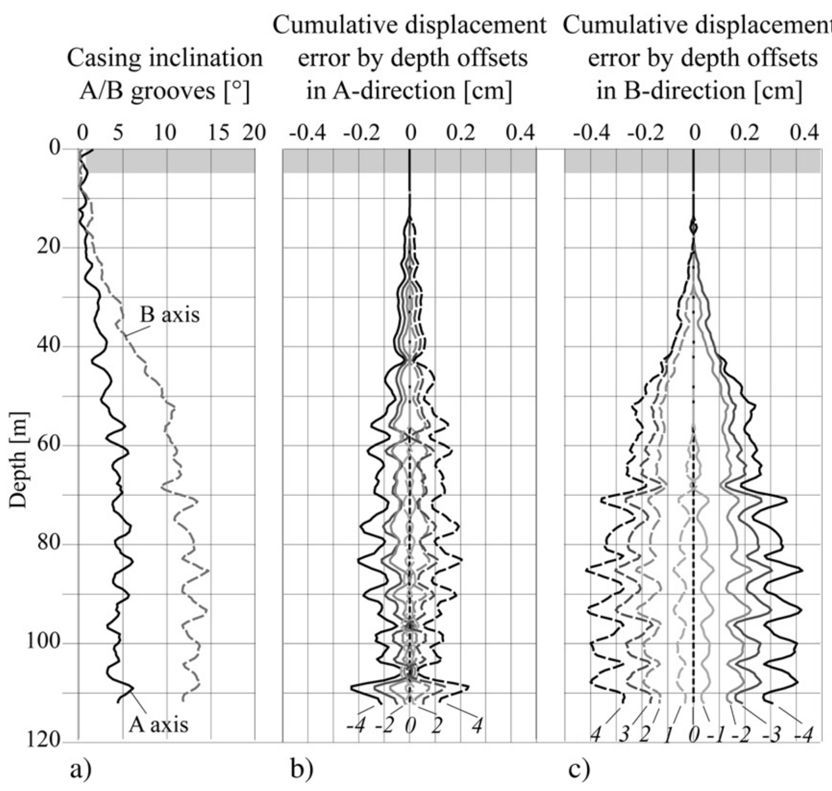

Fig. A-2. Illustration of the effect of depth-offset error on estimated cumulative horizontal displacements. a) Inclination profiles along the *A*- and *B*-axis for the initial survey. b) Cumulative horizontal displacements in the *A*-axis direction obtained between the initial survey and the same initial survey offset by various constant amounts (±5 cm in steps of 1 cm). Note that the displacements are fictitious and arise solely because of the depth-measurement error. c) Same as b) but for the *B*-axis direction.

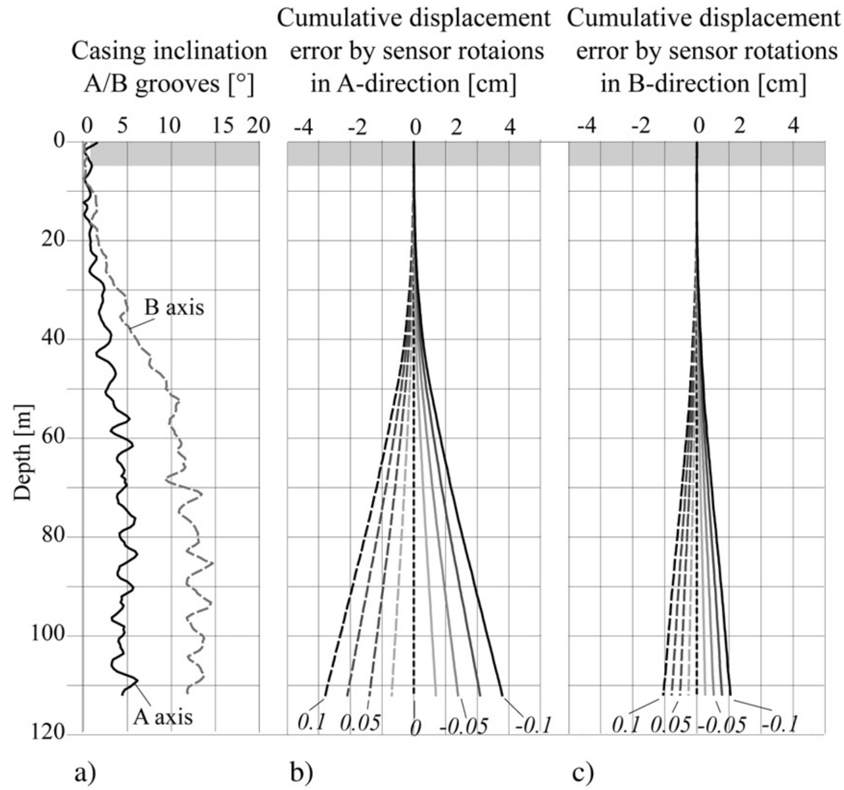

Fig. A-3. Illustration of the effect of sensor-rotation error on estimated cumulative horizontal displacements in SB 120. a) Inclination profiles along the *A*- and *B*-axIs for the initial survey. b) Cumulative horizontal displacements in the *A*-axis direction obtained between the initial survey and the same survey but with inclinations resolved in groove directions rotated from the original survey by various constant amounts (up to 0.1° in steps of 0.025°) to simulate small changes in the orientation of the sensors. Thus, the displacements are fictitious and arise solely because of the simulated change in sensor orientation. c) Same as b) but for the *B*-axis direction.

depth, where the inclination of the hole exceeds 10° (Fig. A-1c). The discrepancy is too large to attribute to measurement error of the spiral-survey probe. Since the azimuthal orientation of the two borehole logs is referenced directly to magnetic north, and thus is reliable, it was concluded that the casing trajectory was in error. We suspect this reflects basic inadequacies in the torsion-survey method of groove orientation determination in situations where the hole is non-vertical and the casing is contorted (Willenberg, 2004). Thus we discarded the torsion survey and instead determined groove orientation with depth by finding the groove orientation which, when applied to the initial inclinometer survey, yielded the well trajectories obtained from the borehole geometry log (Fig. A-1c). The fitting procedure used to produce this 'empirical trajectory' was carried out for wavelengths longer than the 7 m periodic fluctuation in casing orientation that reflects its buckling.

A.2. Depth matching

Mikkelsen (2003) noted that strain occurring along the borehole axis, for example due to slip on fractures, would produce a change in the depth of the fiducial points used in the initial inclinometer survey (he referred to this as 'settlement error'). Thus repeat surveys that used the same 'depth along hole' points would be slightly misaligned. Similar effects can arise from different stretching of the measurement cable used to lower and raise the probe in repeat surveys, although in this case the offset would tend to increase linearly with depth along the borehole. The cables invariably develop kinks and twists when coiled for storage and transportation. A linearly-increasing offset (i.e. uniform stretch) is consistent with this type of depth positioning error. The effect of depth-offset error on the data from SB 120 is illustrated in Fig. A-2. The plots show the fictitious cumulative displacements that result solely from offsetting the initial survey by a constant amount. The magnitude of the depth-offset error increases with local deviation of the casing from vertical, and is exacerbated in SB 120 by the short-wavelength buckling of the casing and the hole deviation from vertical (Fig. A-2a). The error can be largely eliminated by ensuring that the measurement locations for the repeat and the initial survey are the same. In boreholes such as the SB 120, where the casing has short-wavelength fluctuations arising from buckling, this can be accomplished by using cross-correlation to find the offset to the depth scale of the repeat survey which produced the best match with the initial survey. It was found necessary to include a linear cable-stretch component to the depth scale of the repeat survey in order to satisfactorily eliminate the error arising from the 7 m wavelength fluctuations.

A.3. Sensor-rotation error

Sensor-rotation error as described by Mikkelsen (2003) was seen to have a major impact on the present study since several anomalous results can be explained by it. The error arises from small changes in the relative alignment of the sensor and the wheel assembly of the inclinometer probe between surveys. The changes are smaller than the tolerance of sensor alignment in the probe which is 0.5° (Mikkelsen, 2003), and may result from shocks and temperature changes during transit, as well as the more obvious sources of probe rebuild or recalibration. Although the error is nominally present when surveying vertical casing, it is most troublesome in inclined boreholes. In such situations, a change in sensor orientation between surveys will lead to a change in the components of absolute casing inclination resolved in the direction of the two groove axes. This will show as an apparent change in inclination of the two axes between the surveys, and will primarily affect the axis orthogonal to the inclined axis, which is the *A*-axis in SB 120 (Fig. A-3). The large apparent displacements of the borehole bottom wrt top illustrate that the cumulative displacement profiles are extremely sensitive to small changes in sensor orientation in the housing. In our case, the error affects mainly the slope of the profile below 35 m depth, whereas the steps would remain unchanged in direction and magnitude. In practice, a quantification of the sensor-rotation error can only be realised if an inclined section of borehole lies in what is known to be stable ground where the displacements should be zero. The displacements measured in SB 120 indicate that this is not the case for the three deep boreholes in question.

References

Baum, R.L., Johnson, A.M., Fleming, R.W., 1988. Measurement of slope deformation using quadrilaterals. US Geological Survey Bulletin 1842, B1–B23.

Berger, J., 1975. A note on thermoelastic strains and tilts. Journal of Geophysical Research 80 (2), 274–277.

Blikra, L.H., Longva, O., Harbitz, C., Lovholt, F., 2005. Quantification of rock-avalanche and tsunami hazard in Storfjorde, western Norway. In: Senneset, K., Flaate, K., Larsen, J.O. (Eds.), Landslides and avalanches ICFL 2005. Taylor & Francis Group, Norway, pp. 57–64.

Bogaard, T.A., Antoine, P., Desvarreux, P., Giraud, A., van Asch, T.W.J., 2000. The slope movements within the Mondorès graben (Drôme, France); the interaction between geology, hydrology and typology. Engineering Geology 55, 297–312.

Brasser, J.P., Gruner, U., 2002. Behebung der Felssturzgefahr bei Innertkirchen durch zwei Grosssprengungen. Felsbau 20 (5), 195–202.

Brückl, E., Parotidis, M., 2005. Prediction of slope instabilities due to deep-seated gravitational creep. Natural Hazards and Earth System Sciences 5 (2), 155–172.

Brückl, E., Brunner, F.K., Kraus, K., 2006. Kinematics of a deep-seated landslide derived from photogrammetric, GPS and geophysical data. Engineering Geology 88 (3–4), 149–159.

Canuti, P., et al., 2002. Landslide monitoring by using ground-based radar differential interferometry. In: Rybár, J., Stemberk, J., Wagner, P. (Eds.), Landslides — First European Conference on Landslides. Balkema, Prague, pp. 523–528.

Colesanti, C., Wasowski, J., 2006. Investigating landslides with space-borne Synthetic Aperture Radar (SAR) interferometry. Engineering Geology 88 (3–4), 173–199.

Crosta, G.B., Agliardi, F., 2002. How to obtain alert velocity thresholds for large rockslides. Physics and Chemistry of the Earth 27, 1557–1565.

Ding, X., Ren, D., Montgomery, B., Swindells, C., 2000. Automatic monitoring of slope deformations using geotechnical instruments. Journal of Surveying Engineering 2000, 57–68 May.

Dunnicliff, J., 1988. Geotechnical Instrumentation for Monitoring Field Performance. John Wiley & Sons Inc., New York. 577 pp.

Eberhardt, E., Stead, D., Coggan, J.S., 2004. Numerical analysis of initiation and progressive failure in natural rock slopes — the 1991 Randa rockslide. International Journal of Rock Mechanics and Mining Sciences 41 (1), 68–87.

Eyer, W., Gubler, H.U., Keusen, H.R., Naef, O. (Eds.), 1998. Frühwarndienste - Stand der Erkenntnisse und Anwendungsbeispiele. Forstliche Arbeitsgruppe Naturgefahren.

Froese, C.R., et al., 2005. Development and implementation of a warning system for the South Peak of Turtle Mountain. In: Hungr, O., Fell, R., Couture, R., Eberhardt, E. (Eds.), Landslide Risk Management. Taylor & Francis Group, Vancouver, pp. 705–712.

Fukuzono, T., 1985. A new method for predicting the failure time of a slope. Procceedings of the IVth International Conference and Field Workshop on Landslides. National Research Centre for Desaster Prevention, pp. 145–150.

Goodman, R.E., Bray, J., 1976. Toppling of rock slopes, rock engineering for foundations and slopes, boulder. ASCE 201–234.

Groneng, G., Nilsen, B., Blikra, L.H., Braathen, A., 2005. The significance of climate on deformation in a rock-slope failure — the Akerneset case study from Norway. In: Hungr, O., Fell, R., Couture, R., Eberhardt, E. (Eds.), Landslide Risk Management. Taylor & Francis Group, Vancouver, pp. 725–729.

Gunzburger, Y., Merrien-Soukatchoff, V., Guglielmi, Y., 2005. Influence of daily surface temperature fluctuations on rock slope stability: case study of the Rochers de Valabres slope (France). International Journal of Rock Mechanics and Mining Sciences 42 (3), 331–349.

Hancock, P.L., 1985. Brittle microtectonics: principles and practice. Journal of Structural Geology 7 (3/4), 437–457.

Harrison, J.C., Herbst, K., 1977. Thermoelastic strains and tilts revisited. Geophysical Research Letters 4 (11), 535–537.

Heincke, B., Green, A., van der Kruk, J., Willenberg, H., 2006a. Semblance-based topographic migration (SBTM): a method for identifying fracture zones in 3-D georadar data. Near Surface Geophysics 4, 79–88.

Heincke, B., et al., 2006b. Characterizing an unstable mountain slope using shallow 2- and 3-D seismic tomography. Geophysics 71 (6), B241–B256.

Hungr, O., Evans, S.G., 2004. The occurrence and classification of massive rock slope failure. Felsbau 22 (2), 16–32.

Imrie, A.S., Moore, D.P., 1993. The use of rock engineering to overcome adverse geology at Revelstoke Dam. In: Hudson, J.A. (Ed.), Comprehensive rock engineering. Pergamon Press, pp. 701–725.

Jaboyedoff, M., Ornstein, P., Rouiller, J.D., 2004. Design of a geodetic database and associated tools for monitoring rock-slope movements: the example of the top of Randa rockfall scar. Natural Hazards and Earth System Sciences 204 (4), 187–196.

Keusen, H.R., 2002. Infrastrukturanlagen in instabilen felsigen Gebirgen — Werkzeuge für das Risikomanagement. Felsbau 20 (5).

Krähenbühl, R., 2004. Temperatur und Kluftwasser als Ursachen von Felssturz. Bulletin Angewandte Geologie 9 (1), 19–35.

LaFonta, J.-G., Beth, M., 2001. Laboratory Testing of In-Place Inclinometers — Part1.

Mikkelsen, P.E., 2003. Advances in inclinometer analysis. In: Myrvoll, F. (Ed.), Field Measurements in Geomechanics. Swets & Zeilinger, Oslo, pp. 555–567.

Mikkelsen, P.E., Wilson, S.D., 1983. Field instrumentation: accuracy performance, automation and procurement. International Symposium on Field Measurements in Geomechanics. Zürich, pp. 251–272.

Moormann, C., 2003. A new study on the reliability and quality assurance of inclinometer measurements. In: Myrvoll, F. (Ed.), Sixth International Symposium on Field Measurements in Geomechanics. Swets & Zeilinger, Oslo, pp. 575–583.

Nichol, S.L., Hungr, O., Evans, S.G., 2002. Large-scale brittle and ductile toppling of rock slopes. Canadian Geotechnical Journal 39, 773–788.

Ornstein, P., Jaboyedoff, M., Rouiller, J.D., 2005. RandaDB: un système de gestion de mesures appliqué a la surveillance des mouvements de versants. Géoline 2005, Lyon, p. 11.

Rose, N.D., Hungr, O., 2007. Forecasting potential rock slope failure in open pit mines using the inverse-velocity method. International Journal of Rock Mechanics and Mining Sciences 44 (2), 308–320.

Sandersen, F., Bakkehoi, S., Hestnes, E., Lied, K., 1996. The influence of meterological factors on the initiation of debris flows, rockfalls, rockslides and rockmass instability. In: Senneset, K. (Ed.), 7th International Symposium on Landslides. Balkema, Trondheim, pp. 97–114.

Simeoni, L., Mongiovi, L., 2003. The problematic management of the displacement monitoring system of a landslide. In: Myrvoll, F. (Ed.), Sixth International Symposium on Field Measurements in Geomechanics. Balkema, Oslo, pp. 673–680.

Spillmann, T., Maurer, H.R., Green, A., Heincke, B., Willenberg, H., Husen, S., 2007a. Microseismic monitoring of an unstable rock mass. Journal of Geophysical Research 112 B, solid earth.

Spillmann, T., et al., 2007b. Characterization of an unstable rock mass based on borehole logs and diverse borehole radar data. Journal of Applied Geophysics 61 (1), 16–38.

Tarchi, D., et al., 2003. Landslide monitoring by using ground-based SAR interferometry: an example of application to the Tessina landslide in Italy. Engineering Geology 68 (1–2), 15–30.

Voight, B., 1989. Relation to describe rate-dependent material failure. Science 243 (4888), 200–203.

Watson, A.D., Moore, D.P., Stewart, T.W., 2004. Temperature influence on rock slope movements at Checkerboard Creek. In: Lacerda, W., Ehrlich, M., Fontoura, S., Sayao, A. (Eds.), International Symposium on Landslides. Balkema, Rio de Janeiro, pp. 1293–1298.

Willenberg, H., 2004. Geologic and kinematic model of a landslide in crystalline rock (Randa, Switzerland). PhD thesis Thesis, Swiss Federal Institute of Technology, Zürich, 184 pp.

Willenberg, H., et al., 2002. Multidisciplinary monitoring of progressive failure processes in brittle rock slopes — concepts and system design. In: Rybár, J., Stemberk, J., Wagner, P. (Eds.), Landslides — First European Conference on Landslides. Balkema, Prague, pp. 477–483.